International Journal of Multiphase Flow 110 (2019) 148–164

Contents lists available at ScienceDirect

International Journal of Multiphase Flow

journal homepage: www.elsevier.com/locate/ijmulflow

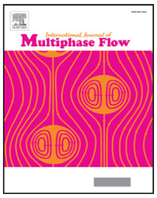

Modeling waves in fluids flowing over and through poroelastic media

Giuseppe A. Zampogna[a,*], Ugis Lācis[b], Shervin Bagheri[b], Alessandro Bottaro[a]

[a] DICCA, Scuola Politecnica, Università di Genova, via Montallegro 1, Genova 16145, Italy
[b] Linné Flow Centre, Department of Mechanics KTH, Stockholm SE-100 44, Sweden

ARTICLE INFO

Article history:
Received 25 May 2018
Revised 18 September 2018
Accepted 19 September 2018
Available online 21 September 2018

Keywords:
Homogenization
Biot-Allard equations
Poroelasticity
Interface conditions

ABSTRACT

Multiscale homogenization represents a powerful tool to treat certain fluid-structure interaction problems involving porous, elastic, fibrous media. This is shown here for the case of the interaction between a Newtonian fluid and a poroelastic, microstructured material. Microscopic problems are set up to determine *effective* tensorial properties (elasticity, permeability, porosity, bulk compliance of the solid skeleton) of the homogenized medium, both in the interior and at its boundary with the fluid domain, and an extensive description is provided of such properties for varying porosity. The macroscopic equations which are derived by homogenization theory employ such effective properties thus permitting the computation of velocities and displacements within the poroelastic mixture for two representative configurations of standing and travelling waves.

1. Introduction

Solid surfaces in nature and technological applications are never perfectly smooth; most often, when a fluid flows above a surface, it encounters a series of (more or less rigid) irregularities, around which it has to move and with which it might interact, whose typical dimensions are often much smaller than those of the macroscopic flow structures present in the fluid domain. Biological surfaces represent an interesting example: they are covered by hair, filaments, scales, feathers, leaves, needles, cilia, etc., which perform a variety of functions. Even if such features are microscopic, their collective effect is often macroscopic, and it is thus justified to try and apply homogenization theory to such porous and compliant media to properly represent their large-scale effects when they interact with a fluid.

If the layer which covers these surfaces is thick, homogenized equations for the medium itself must be established and solved, before the coupling with the fluid above can be attempted. Situations in which poroelastic media of *large dimensions* interact with a fluid abound, ranging from the growth of tumor cells (Penta and Ambrosi, 2013) to the waving of canopies (Nepf, 2012). Another interesting poroelastic medium is that formed by the plumage of birds; Sarradj et al. (2011) studied how the owl hides its acoustic signature thanks to its feathers, composed by barbs, barbules and barbicels of varying dimensions (Bachmann et al., 2008). The hierarchical structure of feathers represents the main feature of homogenization: the typical pores (or the size of the solid inclusions) of the medium must be much smaller than a characteristic dimension of the flow, for multiple scale theory to hold. Thus, microscopic equations can be set up and used to solve for the flow and the structure at small scale in the poroelastic layer (PEL, in the following), yielding tensorial quantities such as effective elasticity or permeability, and companion macroscopic simulations must be conducted in both the fluid and the PEL. These simulations are based on a macroscopic model given by the homogenization itself, which takes into account the couple solid-fluid as a single continuum. This is the idea behind the first works in poroelasticity, such as that by Terzaghi (1936), where an *effective stress* tensor to quantify consolidation and fracture of soils has been introduced. Later, Biot (1955) characterized a poroelastic medium via an *effective elasticity* tensor. These works were based on heuristic considerations. Among the early works which attempted a formal mathematical derivation of Biot's system, we cite the works of Auriault and Sanchez-Palencia (1977) and Burridge and Keller (1981) where the governing equations have been deduced from the pore-scale behavior of the coupled fluid-solid system via an upscaling technique in the quasi-static case. Later, several contributions of Mikelić and collaborators (Jäger et al., 2011; Mikelić and Wheeler, 2012, cf., for istance,) have been devoted to a mathematical formal development of both the quasi-static and the dynamic Biot equations, via the use of homogenization and asymptotic expansions.

---

[*] Corresponding author.
E-mail address: giuseppe.zampogna@edu.unige.it (G.A. Zampogna).

https://doi.org/10.1016/j.ijmultiphaseflow.2018.09.006

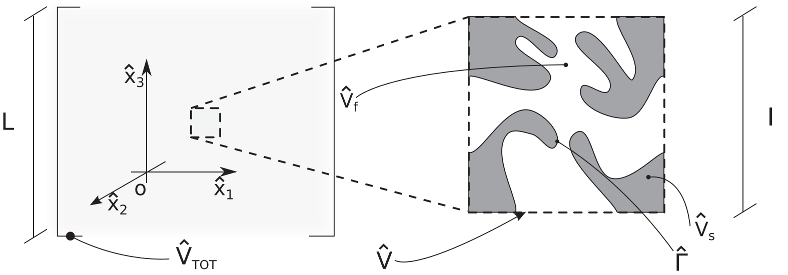

Fig. 1. Macroscopic configuration of a poroelastic matrix and microscopic zoom over one microstructure inside a cubic representative elementary volume $\hat{V}$ (defined by the upscaling technique). L and l are the macroscopic and microscopic length scales; $\hat{V}_s$ and $\hat{V}_f$ are the regions, inside $\hat{V}$, occupied by the solid and the fluid, respectively, and $\hat{\Gamma}$ is the fluid-structure interface within $\hat{V}$.

Since the objective of the present paper is to propose a model to analyze cases where there is an interaction between a free-fluid region and a PEL-region, the determination of the matching conditions between the two regions is fundamental. As pointed out by Shavit (2009), the coupling between a free-fluid region and a porous – or a poroelastic – domain represents a delicate problem, one of the difficulties consisting in the fact that the two domains are treated with different approaches (pointwise equations on the one side and averaged equations on the other), and a unified one-equation theory is not yet universally accepted because of difficulties in satisfying necessary length-scale constraints while volume-averaging across the dividing surface. Theoretical studies involving homogenization across interfacial regions, by matching asymptotic expansions, have however been pursued. In particular, Nevard and Keller (1997) have shown that if we consider an elastic microstructured material, whose properties change suddenly across an irregular interface located within the material itself, it is possible to match the asymptotic expansions valid on either side of the interface to obtain a modified equation which holds in a thin interfacial layer. Adopting the same philosophy, and supported by the theoretical studies of Jäger and Mikelić (1996) and Mikelić and Jäger (2000), Lācis and Bagheri (2016) and Lācis et al. (2017) have recently proposed – and validated in the Stokes flow limit – an interface condition based on homogenization, similar to that developed by Carraro et al. (2015) with different arguments. Such condition represents the generalization of that by Beavers and Joseph (1967), developed to treat the interface between a free-fluid region and a rigid porous medium, without however the need for *ad hoc* parameters, since effective coefficients are available from the solution of auxiliary, microscale problems. In the present paper, this condition is used to handle the interface between a poroelastic medium and a fluid domain ruled by the Navier-Stokes equations, when inertia in the free-fluid region is not negligible.

The paper starts by describing microscopic and macroscopic equations to treat fluid-structure interaction problems, when a free-fluid region is in contact with a fluid-saturated poroelastic medium, developed on the basis of the previously cited papers on upscaling techniques. The model equations rely on a multiple-scale expansion, both for the interior of the PEL and for its interface with the fluid domain, Γ_I. The microscopic problems arising from homogenization, once the scaling parameters are properly set, are described in detail and solved for a range of porosities, when the medium is composed by both fiber-like and sphere-like structures. The significance of the effective properties of the PEL is highlighted. Once they are known, such effective properties are used in the solution of macroscopic problems characterized by the presence of waves, in the presence of flow inertia.

2. A multiscale mathematical model for poroelastic lattices

A continuum model for the fluid-solid mixture denoted in Fig. 1 as $\hat{V}_{TOT}$ is described. In such a macroscopic domain, an elastic porous skeleton of density ρ_s is saturated by an incompressible Newtonian fluid of density ρ_f and viscosity μ; $\hat{V}_{TOT}$ can be decomposed, at least far from its boundaries, in elementary cells over which the structure can be approximated as periodic, as sketched in Fig. 1. Although the elementary cell is fixed in time, $\hat{t}$, its fluid and solid portions depend on time because of the deformation so that, in general, it follows that

$$\hat{V}(\hat{\mathbf{x}}) = \hat{V}_s(\hat{\mathbf{x}}, \hat{t}\,) \cup \hat{V}_f(\hat{\mathbf{x}}, \hat{t}\,), \tag{1}$$

where the dependence on the centroid $\hat{\mathbf{x}}$ of each cell is due to the non homogeneous conditions enforced at the boundaries of the macroscopic poroelastic region (the $\hat{\ }$ denotes a dimensional variable); for ease of notation we will omit both of these dependencies. The equation for the solid motion in the unit cell must be coupled with the equations for the fluid. Thus, we consider the dimensional equation for the structure, in the Lagrangian formulation, i.e.

$$\rho_s \frac{\partial^2 \hat{v}_i}{\partial \hat{t}^2} = \frac{\partial \hat{\sigma}_{ij}}{\partial \hat{x}_j} \quad \text{on } \hat{V}_s, \tag{2}$$

where $\hat{v}_i$ are the components of $\hat{\mathbf{v}}$, the solid displacement vector, and $\hat{\sigma}_{ij}$ are the components of the solid stress tensor. Under the assumption that the structure is elastic, for small strain the following linear equations hold

$$\hat{\sigma}_{ij} = \hat{C}_{ijkl}\hat{\varepsilon}_{kl}(\hat{\mathbf{v}}) = \frac{1}{2}\hat{C}_{ijkl}\left(\frac{\partial \hat{v}_k}{\partial \hat{x}_l} + \frac{\partial \hat{v}_l}{\partial \hat{x}_k}\right), \tag{3}$$

with $\hat{C}_{ijkl}$ the fourth order stiffness or elasticity tensor, whose components depend linearly on Young's modulus of elasticity, E, and on the Poisson ratio, ν_P, for a solid skeleton formed by an isotropic material. In the remainder of the paper, C_{ijkl} is the dimensionless counterpart of $\hat{C}_{ijkl}$, using E as scale. Also, we will fix the value of the Poisson ratio at 0.33 so that in Voigt's contracted notation (Voigt, 1889) the isotropic stiffness tensor of the material forming the solid skeleton is

$$C_{ijkl} = \begin{pmatrix} 1.48 & 0.73 & 0.73 & 0 & 0 & 0 \\ 0.73 & 1.48 & 0.73 & 0 & 0 & 0 \\ 0.73 & 0.73 & 1.48 & 0 & 0 & 0 \\ 0 & 0 & 0 & 0.38 & 0 & 0 \\ 0 & 0 & 0 & 0 & 0.38 & 0 \\ 0 & 0 & 0 & 0 & 0 & 0.38 \end{pmatrix}. \tag{4}$$

Eq. (2) must be coupled to the dimensional Navier-Stokes equations (NSE) which, in the Eulerian formulation can be written in terms of the velocity field $\hat{\mathbf{u}}$ and the pressure field $\hat{p}$, as:

$$\rho_f\left(\frac{\partial \hat{u}_i}{\partial \hat{t}} + \hat{u}_j \frac{\partial \hat{u}_i}{\partial \hat{x}_j}\right) = \frac{\partial \hat{\Sigma}_{ij}}{\partial \hat{x}_j} \quad \text{on } \hat{V}_f, \tag{5}$$

$$\frac{\partial \hat{u}_i}{\partial \hat{x}_i} = 0 \quad \text{on } \hat{V}_f, \tag{6}$$

where $\hat{\Sigma}_{ij}$ is the canonical fluid stress tensor

$$\hat{\Sigma}_{ij} = -\hat{p}\delta_{ij} + 2\mu\hat{\varepsilon}_{ij}(\hat{\mathbf{u}}), \tag{7}$$

with $\hat{\varepsilon}$ the strain tensor for the fluid, formally defined like for the structure. The boundary conditions on the solid-fluid interface $\hat{\Gamma}$ within the poroelastic medium are the continuity of velocity and traction vectors:

$$\hat{u}_i = \frac{\partial \hat{v}_i}{\partial \hat{t}} \quad \text{and} \quad \hat{\Sigma}_{ij}n_j = \hat{\sigma}_{ij}n_j, \tag{8}$$

where $\mathbf{n}$ is the unit vector normal to boundary, pointing from the solid to the fluid domain; moreover, we impose periodicity over all boundaries of the microscopic reference volume $\hat{V}$.

At this point we invoke the separation of scales between L and l (cf. Fig. 1), which allows to define the small parameter $\epsilon = l/L \ll 1$ and to introduce two non-dimensional variables: the microscopic fast variable, $\mathbf{x} = \hat{\mathbf{x}}/l$, and the macroscopic slow variable, $\mathbf{x}' = \epsilon\mathbf{x}$. The use of homogenization theory (Hornung, 1996; Mei and Vernescu, 2010) leads us to macroscopic governing equations via the use of spatial averaging over $\hat{V}$:

$$\langle \cdot \rangle = \frac{1}{|\hat{V}|}\int_{\hat{V}} \cdot \, d\hat{V}. \tag{9}$$

The macroscopic description at leading order of the anisotropic, compressible skeleton's displacement field $\mathbf{v}(\mathbf{x}', t)$ and of the fluid pressure field $p(\mathbf{x}', t)$, whose mathematical development is detailed in Appendix A, is given by

$$\begin{cases} (1-\theta)\frac{\rho_s}{\rho_f}\mathrm{Ca}\ddot{v}_i = \frac{\partial}{\partial x'_j}\left[\mathbb{C}_{ijpq}\varepsilon'_{pq}(\mathbf{v}) - \alpha'_{ij}\mathrm{Ca}\, p\right] & \text{on } V_{TOT}, \\ \beta\mathrm{Ca}\dot{p} - \epsilon^2\mathrm{Re}_L\mathcal{K}_{ij}\frac{\partial^2 p}{\partial x'_j \partial x'_i} = -\alpha_{lk}\frac{\partial \dot{v}_l}{\partial x'_k} & \text{on } V_{TOT}. \end{cases} \tag{10}$$

These equations contain all the dominant terms; the presence of an ϵ^2 term is only related to the fact that they have been made dimensionless by the same scales used in the free fluid region bordering the PEL, namely the characteristic velocity within the free fluid domain, $\bar{U}$, the macroscopic length scale, L, the dynamic pressure, $\rho_f\bar{U}^2$, and the time scale $L/\bar{U}$. We have chosen these scales only for numerical convenience, because of the subsequent need to couple the PEL equations to those ruling the dynamics in the free fluid region. The Reynolds number is $\mathrm{Re}_L = \rho_f\bar{U}L/\mu$ and the Cauchy number is $\mathrm{Ca} = \rho_f\bar{U}^2/E$. In (10) the porosity $\theta = |V_f|/|V|$ appears. The quantity $(1-\theta)\frac{\rho_s}{\rho_f}\mathrm{Ca}$ plays the role of the non-dimensional Biot's density and differs from the classical one since, with the normalizations adopted in the present paper, the time derivative of the fluid velocity is negligible to leading order. Some tensors which vary only over the macroscale are present; they are the *effective elasticity tensor*, $\mathbb{C}_{ijkl}$, the *effective fluid volume fractions*, α_{lk} and α'_{ij}, the *effective permeability tensor*, $\mathcal{K}_{ij}$ and the *bulk compliance of the solid skeleton*, β. All of these tensors (aside from $\mathcal{K}_{ij}$) depend on two further tensors, χ_i^{pq} and η_i, which are defined on the periodic elementary volume V and satisfy the systems:

$$\begin{cases} \frac{\partial}{\partial x_j}\left\{C_{ijkl}\left[\varepsilon_{kl}(\boldsymbol{\chi}^{pq}) + \delta_{kp}\delta_{lq}\right]\right\} = 0 & \text{on } V_s, \\ \left\{C_{ijkl}\left[\varepsilon_{kl}(\boldsymbol{\chi}^{pq}) + \delta_{kp}\delta_{lq}\right]\right\}n_j = 0 & \text{on } \Gamma, \end{cases}$$

$$\begin{cases} \frac{\partial}{\partial x_j}\left[C_{ijkl}\ \varepsilon_{kl}(\boldsymbol{\eta}) + \delta_{ij}\right] = 0 & \text{on } V_s, \\ \left[C_{ijkl}\ \varepsilon_{kl}(\boldsymbol{\eta}) + \delta_{ij}\right]n_j = 0 & \text{on } \Gamma. \end{cases} \tag{11}$$

By using the dimensionless form of (9), the effective elasticity tensor is defined as:

$$\mathbb{C}_{ijpq} = \langle C_{ijkl}\ \varepsilon_{kl}(\boldsymbol{\chi}^{pq})\rangle + \langle C_{ijpq}\rangle, \tag{12}$$

where C_{ijkl} is given by Eq. (4). The first effective fluid volume fraction of the anisotropic skeleton is

$$\alpha_{lk} = \theta\delta_{lk} - \frac{1}{2}\langle\frac{\partial \chi_i^{pq}}{\partial x_i}\rangle(\delta_{lp}\delta_{kq} + \delta_{lq}\delta_{kp}); \tag{13}$$

this form of α_{lk} generalizes the concept introduced for isotropic media by Skotheim and Mahadevan (2004). The vector η_i is used to define the second effective fluid volume fraction, i.e.

$$\alpha'_{ij} = \theta\delta_{ij} + \langle C_{ijkl}\ \varepsilon_{kl}(\boldsymbol{\eta})\rangle, \tag{14}$$

plus the bulk compliance of the solid skeleton

$$\beta = \langle\frac{\partial \eta_i}{\partial x_i}\rangle. \tag{15}$$

It has been shown by Mei & Vernescu (2010) that the two volume fractions coincide, i.e. $\alpha_{ij} = \alpha'_{ij}$ and this is verified in the present paper as a check of numerical consistency. As explained by Showalter (2003), the terms linked to α_{ij} and α'_{ij}, respectively $\alpha_{lk}\frac{\partial \dot{v}_l}{\partial x'_k}$ and $\frac{\partial}{\partial x'_j}\alpha'_{ij}\mathrm{Ca}\, p$, represent the *pore fluid content* due to the local volume change of the pores and the *pressure stress* of the pore fluid on the structure. To close (10) the permeability tensor $\mathcal{K}_{ij} = \langle K_{ij}\rangle$ needs to be defined; it arises from the solution of a Stokes problem over the fluid domain V_f:

$$\begin{cases} \frac{\partial A_j}{\partial x_i} - \frac{\partial^2 K_{ij}}{\partial x_k \partial x_k} = \delta_{ij} & \text{on } V_f, \\ \frac{\partial K_{ij}}{\partial x_i} = 0 & \text{on } V_f, \\ K_{ij} = 0 & \text{on } \Gamma. \end{cases} \tag{16}$$

Once (10) is solved, the fluid velocity over V_{TOT} can be recovered from Darcy's law:

$$\langle u_i\rangle - \theta\dot{v}_i = -\epsilon^2\mathrm{Re}_L\mathcal{K}_{ij}\frac{\partial p}{\partial x'_j} \tag{17}$$

for the effective velocity of the homogenized medium, $\langle u_i\rangle - \theta\dot{v}_i$.

It is important to keep in mind the difference between the model proposed in the present work and those available in the literature to simulate the behaviour of poroelastic media. To make comparisons, we refer to the work of Mikelić and Wheeler (2012) where the dynamic Biot-Allard and the quasi-static Biot models have been formally developed by multiple scale expansions. In the Biot-Allard equations, time integrals are present, accounting for a "memory effect" in the behaviour of the structure. These integrals derive from the fact that in the full dynamic system the equation corresponding to (A.20) contains also the time-derivative of the fluid velocity, implying that the corresponding microscopic system (16) is time-dependent. In the derivation presented in Appendix A the convective term is absent at order ϵ in the fluid momentum equation, because of the chosen scalings. For this reason, the right-hand-side of our Eq. (17) does not contain the time-convolution between the permeability and the pressure gradient, but the simple product of them. Upon substitution of the dynamic counterpart of Eq. (17) into Eq. (A.47) and (A.51), the Biot-Allard model would result (Mikelić and Wheeler, 2012). It should also be noted that the quasi-static Biot system does not take into account the acceleration term on the left-hand-side of the first equation of system (10). Thus, the present model is intermediate between the Biot-Allard and the quasi-static Biot systems: it still allows a dynamic motion of the poroelastic medium, without however exhibiting long-term memory effects. For ease of notation, from this moment on, we refer to the system formed by (10) and (17) as the FPEL (Fluid-PoroELastic) model. It should be stressed again that the FPEL equations, as given here, are made dimensionless, and later solved numerically, using the free fluid scales, and this for immediate coupling at the interface with the dimensionless Navier-Stokes equations.

2.1. Focus on the macroscopic interface

When a poroelastic material is in contact with a macroscopic domain only filled by fluid, it is convenient to introduce a sharp

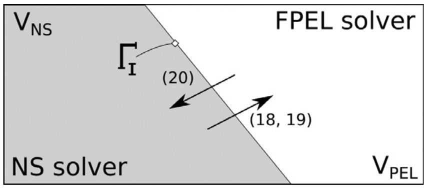

Fig. 2. A pure fluid region and a composite region (V_{NS} and V_{PEL}, respectively) in contact through the fluid-structure macroscopic interface Γ_I. Information between the NS and FPEL solvers is exchanged using Eqs. (18)–(19).

interface between these two domains, which we denote as Γ_I (defined in Fig. 2). In order to solve for the displacement of the poroelastic material and for the pore pressure we need essentially two boundary conditions, one for each equation from system (10). For the elasticity equation we use the stress continuity condition, which has been shown to work well for Stokes flows (Lācis et al., 2017):

$$T_{ij}n_j\big|_{\Gamma_I} = \Sigma_{ij}n_j, \tag{18}$$

where Σ_{ij} is the stress tensor of the free fluid, and T_{ij} is the stress tensor of the mixture in the interior domain (cf. Eq. (A.43) in Appendix A). Same condition has been also proposed previously by Gopinath et al. (2011). For the pore pressure equation we use a Dirichlet condition on the pore-pressure value. There is no agreement in the literature on whether the pressure should be the same as in free fluid (Lācis and Bagheri, 2016) or there should be a jump in pressure (Carraro et al., 2013). In the current work, we select the pressure continuity condition:

$$p^- = p, \tag{19}$$

where p is the free fluid pressure and p^- is the pore pressure directly below the interface. It has been shown by Lācis et al. (2017) that pressure continuity works well for given geometries in poroelastic set-ups. One can also expect pressure continuity for symmetry reasons (Carraro et al., 2013).

To close the formulation, one also needs boundary conditions for the free fluid. For the standard Navier-Stokes equations it is sufficient to provide velocity boundary conditions. The generalized Beavers & Joseph boundary condition (Lācis et al., 2017) for poroelastic materials reads, in non-dimensional form

$$\langle u_i\rangle|_{\Gamma_I} = \dot{v}_i - \epsilon^2 \mathrm{Re}_L \bar{\mathcal{K}}_{ij}\frac{\partial p}{\partial x'_j} + \epsilon \bar{\mathcal{L}}_{ijk}\left(\frac{\partial u_j}{\partial x'_k} + \frac{\partial u_k}{\partial x'_j}\right), \tag{20}$$

where the bars above the unknown tensors denotes that they are obtained using volume averages above the interface in an elongated interface cell (Lācis et al., 2017) near the boundary between the poroelastic medium and the free fluid (see later Figs. 10 and 11). Eq. (20) represents the extended version of the Navier's slip condition. The coefficients arising in the velocity boundary conditions are then found as

$$\bar{\mathcal{K}}_{ij} = \frac{1}{V}\int_{V_I} \tilde{K}_{ij}\, dV, \tag{21}$$

$$\bar{\mathcal{L}}_{ijk} = \frac{1}{V}\int_{V_I} L_{ijk}\, dV, \tag{22}$$

where V_I is the averaging volume in the interface cell.

A simpler form of the interface condition above was found semi-empirically by Beavers and Joseph (1967), and later formally justified by Saffman (1971) and Jäger and Mikelić (1996, 2000, 2009) on the basis of matched asymptotic expansions. Extensions of the condition have been proposed by Jones (1973) and Nield and Bejan (2013) for curved interfaces, by expressing the slip velocity at the dividing surface in terms of the rate of strain. The one proposed here is, to the knowledge of the authors, the most general version of the condition by Beavers & Joseph, and is applicable to any interface between a fluid region and a homogeneous poroelastic medium with an arbitrary microscopic structure, provided the effective solid displacement is sufficiently small for the interface Γ_I to non display appreciable nonlinear deformations.

We refer to Lācis et al. (2017) for the development of (20), which is used for the first time here in the case of *unsteady* interactions between a free-fluid region and a poroelastic region. For the sake of completeness, the interface cell problems are outlined in Appendix B. A set of conditions similar to 18–(20) has been used by Bukač et al. (2015) and Badia et al. (2009) to study the fluid flow across an interface with a poroelastic medium; whereas they imposed effective parameters at the interface by using order of magnitude estimates, we will extract them from the numerical solution of microscopic, auxiliary problems.

3. Microscopic problems

In this section the solutions of the microscopic problems (11) and (16) for the internal region of the poroelastic medium, and of problems (B.1–B.3) for the interfacial region are presented. With the scales chosen to normalize the microscopic equations the problems for the solid and fluid phases are decoupled to leading order at the pore-scale level. We have focussed on two kinds of microscopic structures, shown in Fig. 3: both are cubic symmetric structures, the former is built starting from an isotropic geometry, composed by spheres linked by transversal cylindrical bars (denoted as "spheres" in the following) and the latter is built starting from a transversely isotropic geometry, composed by a main vertical cylinder aligned along x_3 and traversed by two slender cylinders with axes parallel to x_1 and x_2 (denoted as "cylinders"). The ratio between the radius r_c of the connecting cylinders and that of the sphere or of the vertical cylinder, r, is here fixed for each porosity ($r_c/r = 0.4$). The limit value of porosity is constrained by the fact that the connected network needs to be permeable in all directions, i.e. the fluid in V_f must be able to flow throughout the grid; this is realized by porosities in the interval (0.04,1) for the case of "spheres" and (0.3,1) for "cylinders". The need of considering fully permeable porous media (i.e. connected fluid regions) has its solid counterpart in the need of using connected skeletons: if this were not the case, there would be no elastic response to a deformation along the direction in which the structure is disconnected (Hoffmann et al., 2004).

The general form of the (symmetric) effective stiffness tensor in Voigt's notation for the microscopic structures examined, is

$$\mathbb{C}_{ijkl} = \begin{pmatrix} \mathbb{C}_{1111} & \mathbb{C}_{1122} & \mathbb{C}_{1133} & 0 & 0 & 0 \\ \mathbb{C}_{1122} & \mathbb{C}_{1111} & \mathbb{C}_{1133} & 0 & 0 & 0 \\ \mathbb{C}_{1133} & \mathbb{C}_{1133} & \mathbb{C}_{3333} & 0 & 0 & 0 \\ 0 & 0 & 0 & \mathbb{C}_{2323} & 0 & 0 \\ 0 & 0 & 0 & 0 & \mathbb{C}_{1313} & 0 \\ 0 & 0 & 0 & 0 & 0 & \mathbb{C}_{1212} \end{pmatrix},$$

with $\mathbb{C}_{2323} = \mathbb{C}_{1313}$ and $\mathbb{C}_{1212} \neq \frac{1}{2}(\mathbb{C}_{1111} - \mathbb{C}_{1122})$ as a consequence of the lateral connecting cylindrical rods. There are thus, at the most, six independent elements. In the "spheres" case the independent terms reduce to three, since $\mathbb{C}_{3333} = \mathbb{C}_{1111}$, $\mathbb{C}_{1122} = \mathbb{C}_{1133}$, and $\mathbb{C}_{1212} = \mathbb{C}_{1313} = \mathbb{C}_{2323}$. This is the case of the simplest possible anisotropic structure, that with cubic symmetry. In the "cylinders" case all six coefficients must be solved for. The transverse isotropy in this case is broken by the presence of the $\mathbb{C}_{1212}$ term, which is independent of $\mathbb{C}_{1111}$ and $\mathbb{C}_{1122}$; the reason is that not all planes through the axis of symmetry x_3 of the main cylinder are planes of symmetry of the whole structure.

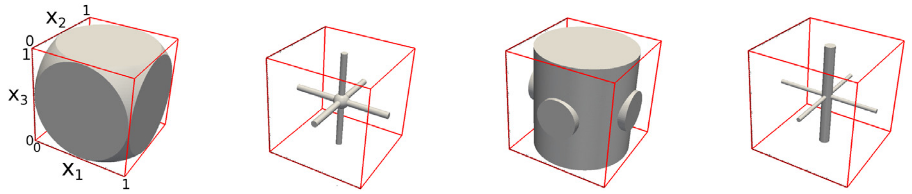

Fig. 3. The two different microscopic structures analyzed in the present work, shown here in the limit case of very small and very large porosities.

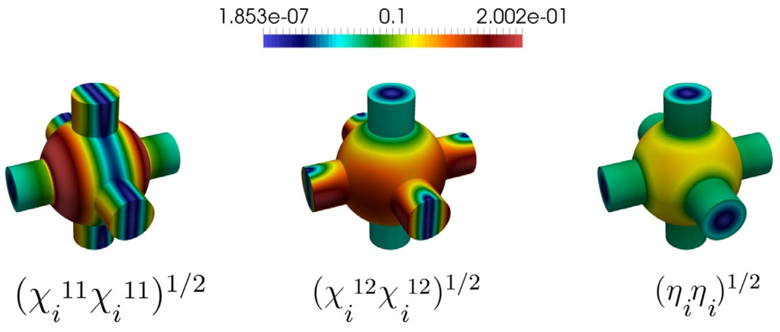

$(\chi_i^{11}\chi_i^{11})^{1/2}$ $(\chi_i^{12}\chi_i^{12})^{1/2}$ $(\eta_i\eta_i)^{1/2}$

Fig. 4. Magnitude of the independent components of $\boldsymbol{\chi}$ in the case of "spheres" for $\theta = 0.8$.

3.1. Solution of the interior problem

A detailed parametric study is presented here for the interior microscopic problem[1] for both the cases of "spheres" and "cylinders", when $r_c/r = 0.4$. Results for other radii ratios are presented by Zampogna and Bottaro (2017).

Attention is initially focussed on problems (11). The magnitude of the independent entries of the microscopic field $\boldsymbol{\chi}$ are represented in Fig. 4 for a set of parameters used later. Since only the components of the average over V_s of the Jacobian of $\boldsymbol{\chi}$ and $\boldsymbol{\eta}$, $J(\boldsymbol{\chi}^{ij})_{kl}$, $J(\boldsymbol{\eta})_{kl}$, $i, j, k, l = 1, 2, 3,$ are present in the macroscopic equations, we need to look at these elements carefully. In the case of "spheres" the non-zero components of $J(\boldsymbol{\chi}^{ij})_{kl}$ and $J(\boldsymbol{\eta})_{kl}$ are listed in the following equations, highlighting their symmetries because of the isotropy of the material and the (cubic) symmetry of the microscopic structure:

$$\begin{aligned}
&J(\boldsymbol{\chi}^{11})_{11} = J(\boldsymbol{\chi}^{22})_{22} = J(\boldsymbol{\chi}^{33})_{33},\\
&J(\boldsymbol{\chi}^{ll})_{kk} = J(\boldsymbol{\chi}^{11})_{22}, \quad l, k = 1, 2, 3, \; l \neq k,\\
&J(\boldsymbol{\chi}^{lk})_{lk} = J(\boldsymbol{\chi}^{lk})_{kl} = J(\boldsymbol{\chi}^{12})_{12}, \quad l, k = 1, 2, 3, \; l \neq k,\\
&J(\boldsymbol{\eta})_{11} = J(\boldsymbol{\eta})_{22} = J(\boldsymbol{\eta})_{33}.
\end{aligned} \tag{23}$$

The values of the four independent coefficients are represented in Fig. 5 for porosities ranging in the interval (0.04, 0.97). Combining Eq. (23) with (12) we obtain that $\mathbb{C}_{ijkl}$ is defined by three independent elements. The sudden slope discontinuity which appears in all the curves in Figs. 5 and 6 close to $1 - \theta = 0.6$ is due to a change in the topology of the main central sphere in the unit cell: for $\theta < 0.4$ the presence of the cylinders to connect the microscopic structure is not needed anymore and V_s can be simply realized via the intersection between a unitary cube and a sphere centered in it. Fig. 6 demonstrates how the skeleton behaves following a deformation: the elastic response (i.e. the intensity of the bulk and shear moduli) becomes smaller when the porosity increases, i.e. when the central sphere is smaller (or when the main cylinders are slender). Moreover, it is important to note that even if we are evaluating a cubic symmetric structure on a cubic elementary cell, the information about the isotropy of the initial geometry, the sphere, is maintained: the relation $\mathbb{C}_{1212} = \mathbb{C}_{1313} = \mathbb{C}_{2323}$ holds, which, in general, is not true for cubic symmetric structures. Even if α_{ij} and α'_{ij} are defined in a completely different way, they assume the same numerical value, since for generic microscopic structures it is

$$\langle \varepsilon_{ii}(\boldsymbol{\chi}^{pq}) \rangle = -\langle C_{pqlk}\varepsilon_{lk}(\boldsymbol{\eta}) \rangle \quad p = q = 1, 2, 3. \tag{24}$$

It should also be noted that the quantities shown in Eq. (24) are of the same order of the porosity itself, especially for intermediate values of θ, so that the effective fluid volume fraction, $\alpha_{ii} = \alpha'_{ii}$, displays changes with respect to the porosity because of compressibility effects. If the compressibility of the material decreases (i.e. ν_P approaches 0.5), $\boldsymbol{\eta}$ and $\boldsymbol{\chi}$ decrease and the difference between θ and $\boldsymbol{\alpha}$ becomes smaller. Focusing on the definitions of $\boldsymbol{\alpha}$ and $\boldsymbol{\alpha}'$ in Eqs. (13,14), we observe that $\boldsymbol{\alpha}$ varies with the porosity because of internal deformations of the structures; such internal deformations are due to external forcing on Γ, whose dependence on θ is measured by $\boldsymbol{\alpha}'$ (cf. Eq. (A.37)). This interpretation of the *effective fluid volume fractions* confirms that the variations with respect to θ are the same for $\boldsymbol{\alpha}$ and $\boldsymbol{\alpha}'$, as stated in (24).

In the "cylinders" case, the magnitude of the independent components of the microscopic field $\boldsymbol{\chi}$ are represented in Fig. 7 for a fixed porosity. In this case, since the initial microscopic structure is transversely isotropic, there are ten independent coefficients of the Jacobians of $\boldsymbol{\chi}$ and $\boldsymbol{\eta}$, listed below and represented in Fig. 8 for varying values of θ:

$$\begin{aligned}
&J(\boldsymbol{\chi}^{11})_{11} = J(\boldsymbol{\chi}^{22})_{22},\\
&J(\boldsymbol{\chi}^{11})_{22} = J(\boldsymbol{\chi}^{22})_{11},\\
&J(\boldsymbol{\chi}^{11})_{33} = J(\boldsymbol{\chi}^{22})_{33},\\
&J(\boldsymbol{\chi}^{33})_{11} = J(\boldsymbol{\chi}^{33})_{22},\\
&J(\boldsymbol{\chi}^{33})_{33},\\
&J(\boldsymbol{\chi}^{lk})_{kl} = J(\boldsymbol{\chi}^{lk})_{lk} = J(\boldsymbol{\chi}^{12})_{12}, \quad l, k = 1, 2, \; l \neq k,\\
&J(\boldsymbol{\chi}^{l3})_{l3} = J(\boldsymbol{\chi}^{3l})_{l3} = J(\boldsymbol{\chi}^{13})_{13}, \quad l = 1, 2,\\
&J(\boldsymbol{\chi}^{3l})_{3l} = J(\boldsymbol{\chi}^{l3})_{3l} = J(\boldsymbol{\chi}^{13})_{31}, l = 1, 2,\\
&J(\boldsymbol{\eta})_{11} = J(\boldsymbol{\eta})_{22},\\
&J(\boldsymbol{\eta})_{33}.
\end{aligned} \tag{25}$$

---

[1] The solution of the interior problem has been carried out using *OpenFoam*, with a solver already described by Zampogna and Bottaro (2017). The numerical convergence of the results has been verified using three different mesh sizes with up to 8×10^6 cells per unit volume. Some results have been independently verified by a solver based on FreeFem++ (Hecht, 2012).

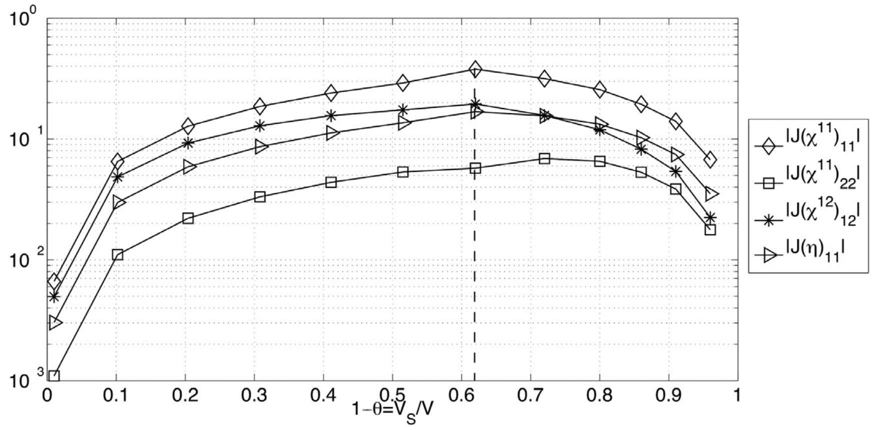

Fig. 5. Absolute values of the four independent parameters identified by Eqs. (23) as function of the solid fraction for the "spherical" microscopic structure.

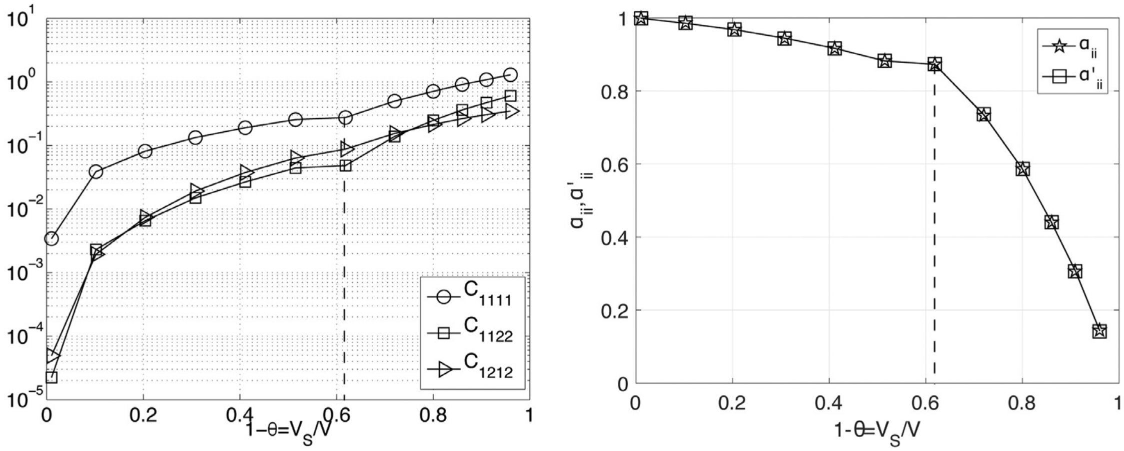

Fig. 6. Components of the effective elasticity tensor $\mathbb{C}_{ijkl}$ (left) and effective fluid volume fractions α_{ij} and α'_{ij} (right) in the case of "spheres".

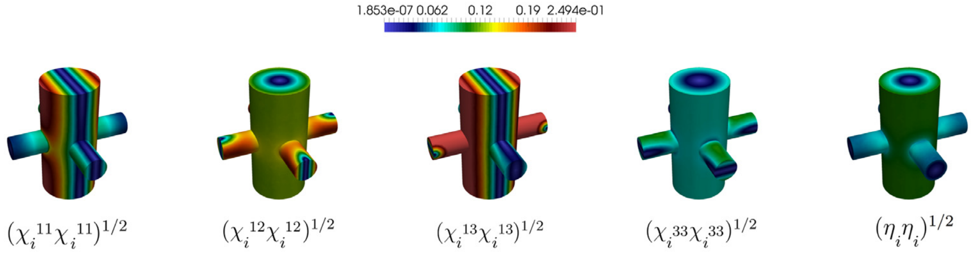

$(\chi_i^{11}\chi_i^{11})^{1/2}$ $(\chi_i^{12}\chi_i^{12})^{1/2}$ $(\chi_i^{13}\chi_i^{13})^{1/2}$ $(\chi_i^{33}\chi_i^{33})^{1/2}$ $(\eta_i\eta_i)^{1/2}$

Fig. 7. Magnitude of the independent components of $\boldsymbol{\chi}$ in the case of "cylinders" for $\theta = 0.8$.

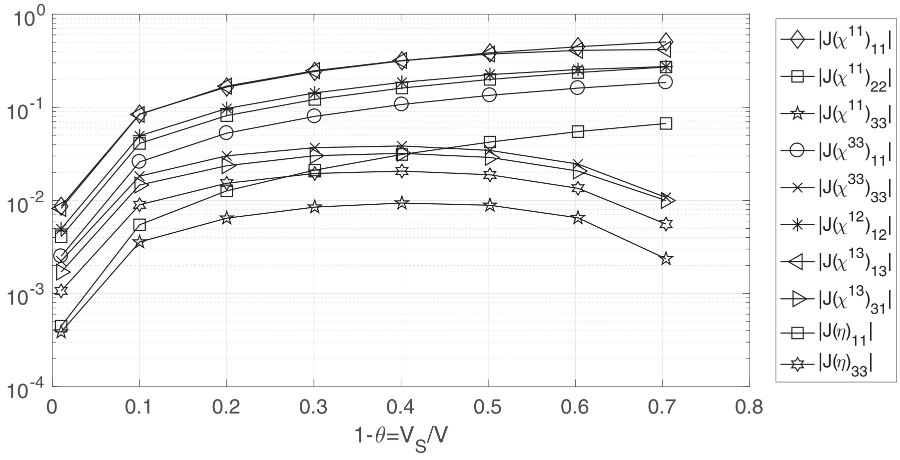

Fig. 8. "Cylindrical" microscopic structure: absolute values of ten independent parameters identified by Eqs. (25) as function of the solid fraction.

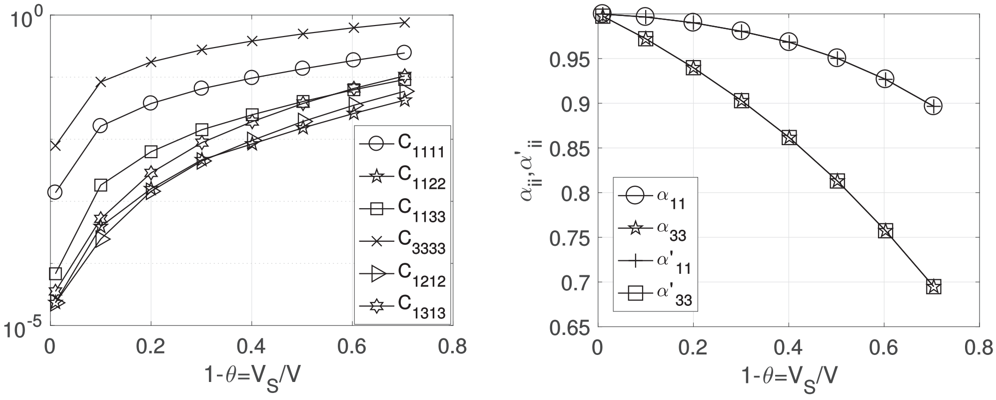

Fig. 9. Non-zero entries of $\mathbb{C}_{ijkl}$ (left), α_{ij} and α'_{ij} (right) for different porosities in the case of "cylinders".

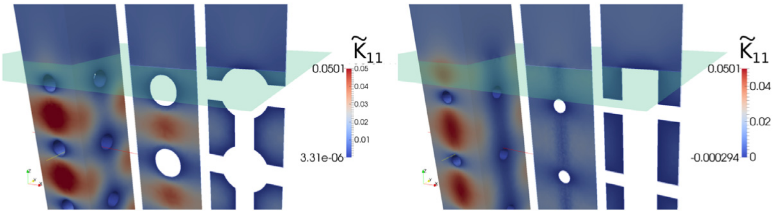

Fig. 10. Solutions of interface problems for the coefficients of the Darcy term. The interface is located exactly at the tip of the last solid structure (green, transparent plane). Porosity $\theta = 0.8$ and radius ratio $r_c/r = 0.4$. "Sphere" (left) and "cylinder" (right) microscale geometries. The plots are cut after the second microstructure below the interface although the full solution domain consists of five microstructures. (For interpretation of the references to colour in this figure legend, the reader is referred to the web version of this article.)

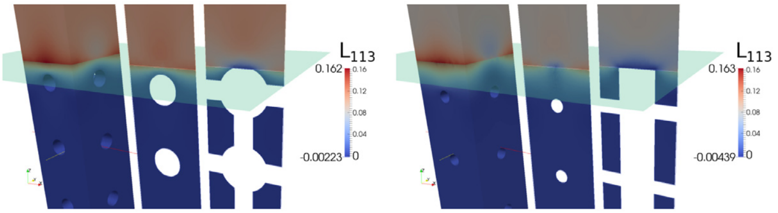

Fig. 11. Solutions of interface problems for the coefficients of the Navier-slip term, for "spheres" (left) and "cylinders" (right).

The components of the effective stiffness tensor are represented in Fig. 9. The considerations valid for the case of "spheres", about the behavior of the elastic response of the structure, hold also in the "cylinders" case. In particular, the information about the transverse isotropy of the starting geometry, the main vertical cylinder, are conserved in the shear modulus, i.e. $\mathbb{C}_{1313} = \mathbb{C}_{2323} \neq \mathbb{C}_{1212}$. Also in the case of "cylinders" α_{ii} and α'_{ii} are equal to within numerical accuracy, as it should be, and this represents a further check on the reliability of the numerics.

Comparing the *effective elasticity tensor*, for both the structures analyzed, in the limit for V_f which approaches zero, the components of the microscopic tensor C_{ijkl} are recovered; furthermore, α_{ij} and α'_{ij} tend to $\theta\delta_{ij}$. This fact can be easily proven by observing that, for $V_f = 0$, Γ disappears and problems (11) become homogeneous, so that $\boldsymbol{\chi}$ and $\boldsymbol{\eta}$ are equal to zero.

3.2. Solution of the interface problem

As for the interior problem, we consider two different geometries for the interface problem[2], "spheres" and "cylinders", but we focus on a single value of the porosity, $\theta = 0.8$, to be later used in all macroscopic simulations. All non-zero components determined from the simulation as volume averages above the interface and volume averages in the periodic unit cell below the interface are summarized in Table 1.

Table 1
Effective tensor components arising from the interface problem. Both geometries are considered.

		$\bar{\mathcal{K}}_{11}$	$\bar{\mathcal{K}}_{33}$	$\bar{\mathcal{L}}_{113}$
"Spheres"	Interface	$1.01 \cdot 10^{-2}$	$1.71 \cdot 10^{-2}$	$1.08 \cdot 10^{-1}$
	Interior	$1.79 \cdot 10^{-2}$	$1.72 \cdot 10^{-2}$	–
"Cylinders"	Interface	$1.31 \cdot 10^{-2}$	$2.51 \cdot 10^{-2}$	$8.79 \cdot 10^{-2}$
	Interior	$1.33 \cdot 10^{-2}$	$2.50 \cdot 10^{-2}$	–

In the current work, since we focus on a two-dimensional macroscopic problem, only the components $\tilde{K}_{11}$, $\tilde{K}_{33}$ and L_{113} are required. The underlying fields for $\tilde{K}_{11}$ are shown in Fig. 10 for both geometries. There we can see that, in both cases, the solution rapidly approaches the periodic interior solution. The interface permeability is obtained as a volume average above the interface location (green plane). For comparison purposes, we give in the table also the interior macroscopic values of the coefficients, evaluated at the second microstructure below the interface as volume average over the representative volume element. Such internal values are identical to those obtained with the procedure described in Section 3.1. Similarly, the underlying fields for L_{113} are shown in Fig. 11 for both geometries. There we see that, for both geometries,

---

[2] The solution of the interface problem has been computed using a *FreeFem++* solver (https://github.com/UgisL/flowMSE).

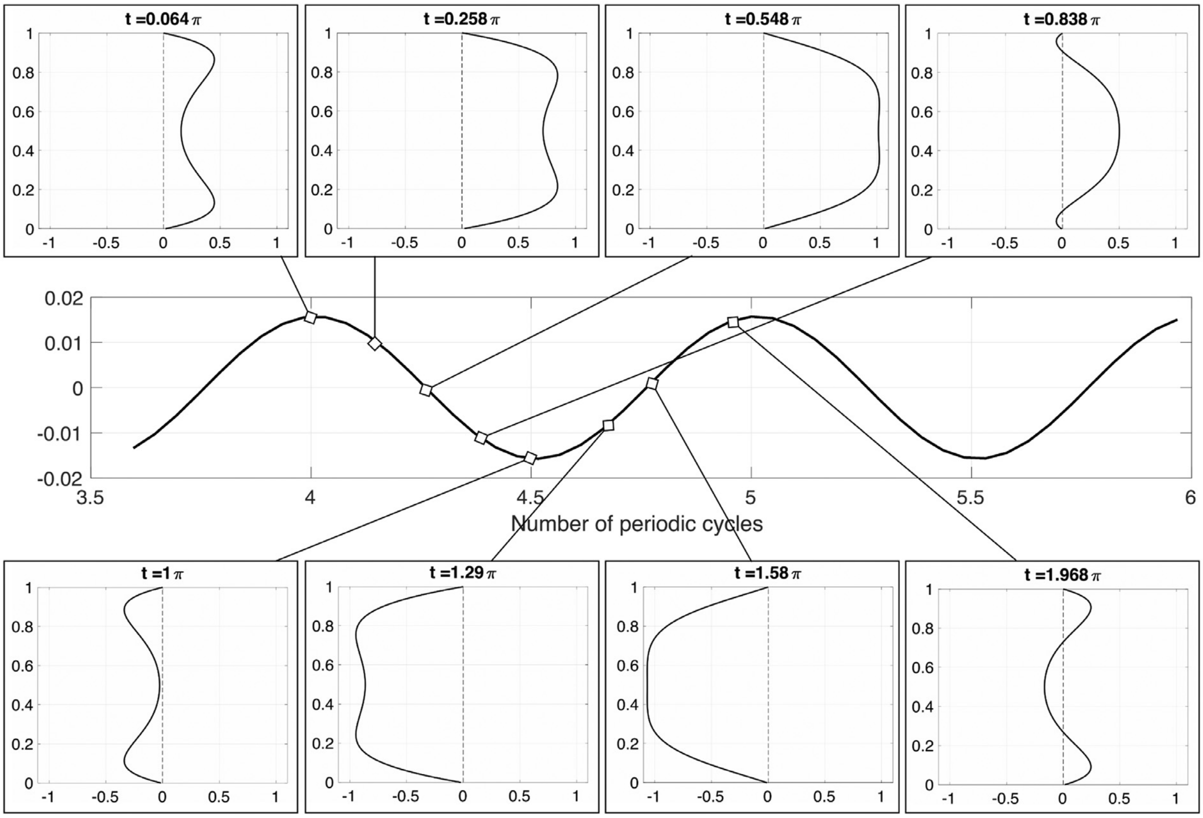

Fig. 12. Central image: mean horizontal component of the effective velocity field in the poroelastic domain as function of time. The insets represent the horizontal velocity profile in the fluid domain at $x_1' = 1$ (midline through the domain), sampled at the instants of the periodic cycle indicated in the central image. Except for a thin layer immediately above the interface, $x_3' = 0$, to this scale the present solution is almost indistinguishable from Womersley's exact solution.

the field rapidly dissipates within the interior, practically reaching a zero value already at the level of the second microstructure.

4. Macroscopic applications

In this section we solve for two different configurations of the flow to show the applicability of the FPEL model to real physical cases. In the first example the relations between the characteristic scales of the fluid and of the structure's motion, which are at the basis of our homogenization approach, are strictly taken into account (cf. Appendix A); in the latter, these scaling relations are weakened to allow us to compare qualitatively the numerical solution of the PEL model with experiments on canopy flows taken from the literature.

4.1. Standing waves

Macroscopic solutions are obtained with a domain-decomposition-based solver, described in Zampogna and Bottaro (2017), whose fundamental idea is to solve iteratively the Navier-Stokes equations within the V_{NS} and the FPEL equations within the V_{PEL} regions, defined in Fig. 2. A two-way coupling between the two regions is performed thanks to the interface conditions, imposed at Γ_I, which is the intersection between the two domains: Eqs. (18) and (19) are used to go from the NS to the PEL domain and Eq. (20) is used in the opposite sense. A validation of the FPEL model for some steady configurations is provided in Zampogna and Bottaro (2017). Here, we aim to understand the time-dependent behavior of the model, and solve an unsteady configuration of the flow, without any further assumption, except for the fact that the unknowns do not depend on the transverse direction, x_2.

The configuration chosen allows to evaluate the horizontal and vertical components of the velocity in V_{NS} and V_{PEL}. In particular, within V_{NS}, a vertical velocity which in the absence of the poroelastic medium would be zero, develops. A channel, of non-dimensional size 2×2, is filled in the upper half by a fluid, and in the lower half by a saturated poroelastic medium with spherical inclusions and porosity equal to 0.8. The motion of the fluid is due to an oscillating pressure gradient which has the dimensionless form: $\partial_1 p(t) = \alpha \cos(\omega t)$. In dimensional terms the box dimensions are taken to be $1\,m \times 1\,m$. The fluid contained within it is an aqueous solution of glycerol at about 98% ($\rho_f = 1250\ kg/m^3$, $\nu = 8 \times 10^{-4}\ m^2/s$, cf. Segur and Obestan, 1951) and, for $\mathrm{Re}_L = \rho_f \bar{U} L/\mu = 100$, the characteristic speed $\bar{U}$ in the pure fluid domain is $0.08\,m/s$. This yields a pressure scale which is of order $P \sim \rho_f \bar{U}^2 = 8\ Pa$ both in the fluid and in the poroelastic region, with a consequent displacement scale of the pores of order $PL/E = 27\ \mu m$ for materials with very low Young's modulus, $E = 3 \times 10^5\ Pa$, such as sylicon-based polymers ($\rho_s = 16\ Kg/m^3$). There is thus a factor of about 10^5 between the scale of the displacement of the pores and the wavelength of the standing wave which is created in the channel. The velocity within the poroelastic medium scales as $U \sim \epsilon^2 PL/\mu$ and, if $\epsilon = 2.14 \times 10^{-2}$, it has a value of order $0.0037\,m/s$ which is about twenty times smaller than the velocity in the pure fluid region. This is clearly related to the Reynolds number and to $\epsilon = l/L$, since it is $U \sim \epsilon^2 \mathrm{Re}_L \bar{U}$ (cf. Appendix A); note also that $\mathrm{Re} \sim \epsilon^3 (\mathrm{Re}_L)^2$ so that the value of the microscopic Reynolds number is of order 0.1, close to the limit of applicability of the theory. The effect of ϵ on the amplitude of the displacement will be examined later on. The Cauchy number which ensues from the parameters chosen is $\mathrm{Ca} = \rho_f \bar{U}^2/E = 2.7 \times 10^{-5}$.

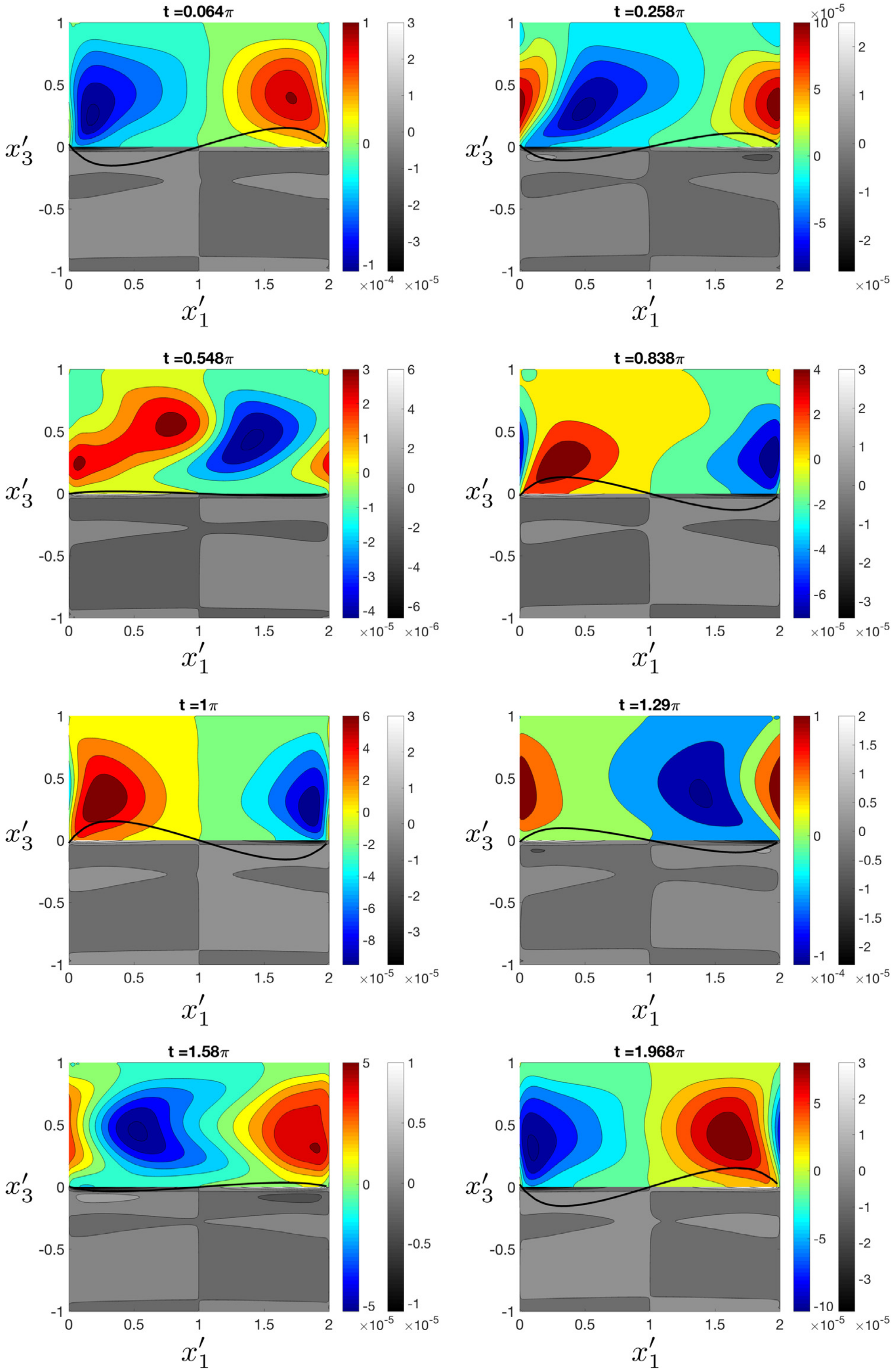

Fig. 13. Contours of the vertical component of the effective velocity field in the whole domain. The periodic cycle is sampled at 8 instants within a period of oscillations. The fluid-structure interface Γ_I is positioned at rest at $x'_3 = 0$. The colors refers to the pure fluid region, V_{NS}, while the grayscale indicates the contours of $\langle u_3 \rangle - \theta \dot{v}_3$ in the V_{PEL} The thick solid lines represent the vertical displacement of the macroscopic interface Γ_I, $(\mathrm{Ca}/2)^{-1} v_3$, for the respective snapshots.

The central image of Fig. 12 shows the horizontal velocity averaged throughout the PEL, as function of time. The dimensionless mean velocity attains values of order 10^{-2}, consistent with the scalings just discussed. In the same figure, eight instants during the periodic cycle are provided for the profile of the horizontal velocity in the free fluid region, sampled at $x'_1 = 1$. At the horizontal interface Γ_I, positioned at $x'_3 = 0$, a weak slip flow arises. The vertical velocity which ensues from the presence of the PEL is drawn in Fig. 13, in both the PEL region and in the free fluid domain; such a component is smaller than its horizontal counterpart and is negligible in the PEL. This is borne out by equation (17) since the imposed pressure gradient acts along x_1. Fig. 13 also displays the standing oscillation of the interface, with the vertical displacement divided by $Ca/2$ for the oscillation to be visible in the scale of the

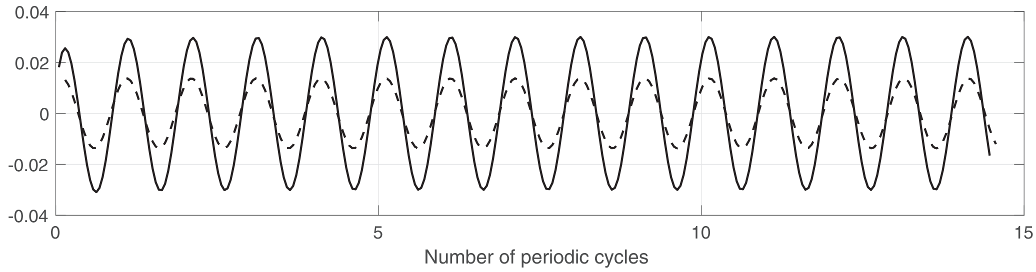

Fig. 14. Mean horizontal fluid velocity at the interface as function of time: comparison between the result of the present work (solid line) and that computed with the simplified condition by Zampogna and Bottaro (2017) (dashed line).

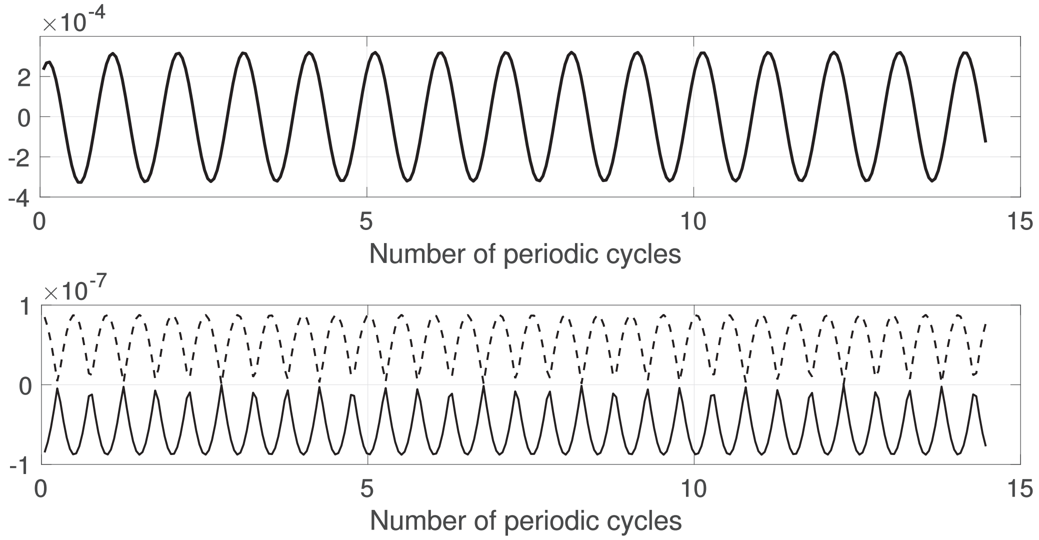

Fig. 15. Top frame: mean horizontal displacement of the interface in time. Bottom frame: maximum and minimum values of the vertical displacement of the interface in time for the same configuration.

figure. In physical dimensions the maximum displacement is very small (consistent with the scalings of the previous paragraph), but the waveform is clear and numerically well resolved.

When the horizontal velocity is averaged over only the interface, a temporal oscillation such as that shown in Fig. 14 appears; after one period the solution has already attained a limit-cycle behavior. Here, the effect of the homogenized boundary condition can be appreciated, since the solid line (current solution) displays the solution obtained by employing Eq. (20), while the dashed line is obtained by treating the interface with the simplified condition ($\bar{\mathcal{L}}_{113} = 0$) used by Zampogna and Bottaro (2017). With the new condition the interface velocity is about 50% larger than with the simplified condition, stressing the importance of an appropriate treatment of the fluid-PEL boundary, with account of both an interfacial permeability, $\bar{\mathcal{K}}_{ij}$, and a tensorial Navier slip length, $\bar{\mathcal{L}}_{ijk}$.

From the point of view of the solid motion, an analysis of the behavior of the skeleton is provided in Fig. 15. The value of the horizontal displacement averaged over the interface is plotted versus time in the top frame. Since the vertical displacement has zero mean, we have chosen to represent the time variation of its maximum and minimum values instead, in the bottom frame of the figure. The dimensionless amplitudes are very small (cf. vertical axes of the figure), conforming to the scales and the normalization chosen. Since the interface Γ_I moves with the pressure gradient which forces the macroscopic flow, its displacement can be written as

$$v_1 = A(x_1')cos(\omega t + \phi_1) \quad \text{and} \quad v_3 = B(x_1')cos(\omega t + \phi_2) \quad \text{at } x_3' = 0 \tag{26}$$

where A and B are amplitudes and ϕ_1, ϕ_2 are *a priori* unknown phases.

It is clear from Appendix A that ϵ is strictly related to Re_L and Ca in order for the homogenization hypotheses to be satisfied. Going beyond the scaling expressed by Eq. (A.6), we have varied ϵ and Ca to examine qualitatively the response of the structure to variations of these two parameters. Fig. 16 shows that the amplitude becomes smaller as ϵ increases. This fact means that the smaller is the characteristic size of the microscopic structure, for given macroscopic scales, the larger is its elastic deformation to an external forcing. Alternatively, an increase of Ca is equivalent to a decrease of Young's modulus E and this provokes a sizeable deformation of the elastic skeleton. This intuitive behaviour can be shown by analyzing the interface conditions expressed by (18), imposed at Γ_I, which are used to transfer information from the fluid region to the PEL. In dimensionless terms they read

$$\mathbb{C}_{1313}\ \varepsilon_{13}(\mathbf{v}) = \frac{\mathrm{Ca}}{\epsilon \mathrm{Re}_L}\ \varepsilon_{13}(\mathbf{u}|_F)$$

and

$$\mathbb{C}_{3311}\ \varepsilon_{11}(\mathbf{v}) + \mathbb{C}_{3333}\ \varepsilon_{33}(\mathbf{v}) - \alpha_{33}\ \mathrm{Ca}\ p|_H = -\mathrm{Ca}\ p|_F + \frac{\mathrm{Ca}}{\epsilon \mathrm{Re}}\ \varepsilon_{33}(\mathbf{u}|_F), \tag{27}$$

with the solid strain at the interface Γ_I which is thus inversely proportional to ϵ and directly proportional to Ca. In conclusion, the deformation of the structure with ϵ and Ca displays a trend which agrees with expectations based on physical arguments.

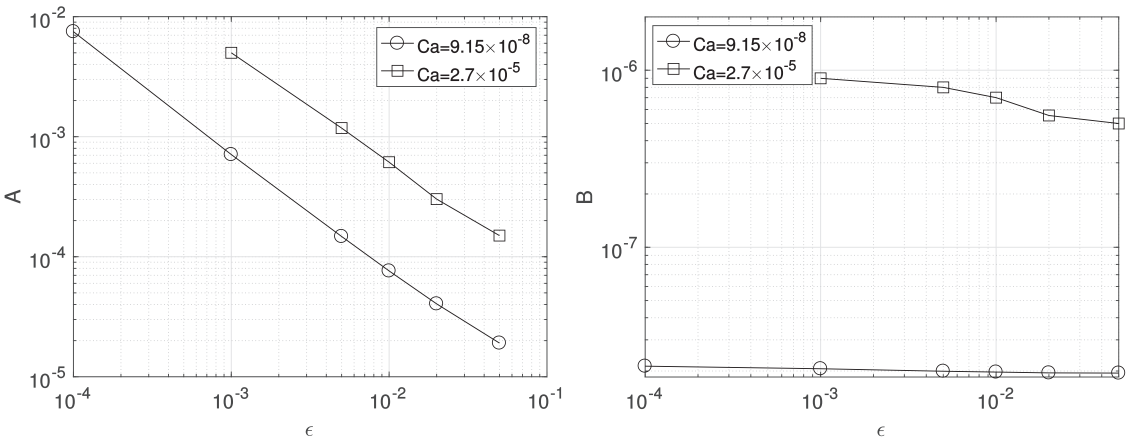

Fig. 16. Maximum, along x_1' and for $x_3' = 0$, of the displacement amplitudes, defined in Eq. (26). For each ϵ two different values of Ca are shown.

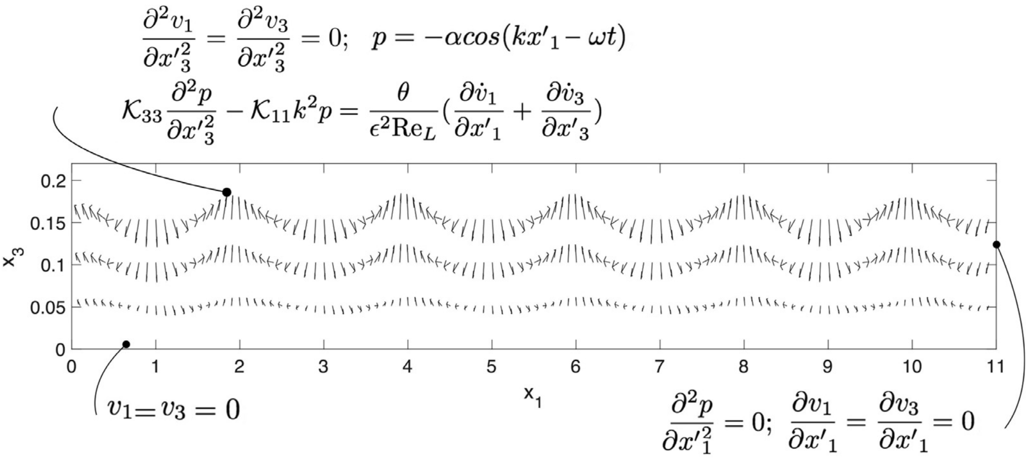

$$\frac{\partial^2 v_1}{\partial x_3'^2} = \frac{\partial^2 v_3}{\partial x_3'^2} = 0; \quad p = -\alpha cos(kx'_1 - \omega t)$$

$$\mathcal{K}_{33}\frac{\partial^2 p}{\partial x_3'^2} - \mathcal{K}_{11}k^2 p = \frac{\theta}{\epsilon^2 \mathrm{Re}_L}\left(\frac{\partial \dot{v}_1}{\partial x'_1} + \frac{\partial \dot{v}_3}{\partial x'_3}\right)$$

$$v_1 = v_3 = 0$$

$$\frac{\partial^2 p}{\partial x_1'^2} = 0; \quad \frac{\partial v_1}{\partial x'_1} = \frac{\partial v_3}{\partial x'_1} = 0$$

Fig. 17. Computational domain together with the boundary conditions employed. The interface between the PEL domain and the free fluid region is positioned at $x_3 = 0.194$. The arrows represents the displacement field at a certain temporal instant. Image not to scale.

4.2. Travelling waves

Alongside the low-Re configuration just shown, a different case, characterized by complex phenomena associated to turbulence, is tested. This case, which stretches the limits of applicability of the model equations, concerns vegetated aquatic flows, common in nature and studied extensively in the past (e.g. Raupach and Shaw, 1982; De Langre, 2008; Ghisalberti and Nepf, 2009; Nepf, 2012). A key point of the cited works consists in modelling the presence of the vegetation and its effect on the fluid flows. A very common choice is to model the drag exerted by the canopy on the fluid in the context of the mixing layer analogy (Raupach and Finnigan, 1996), introducing a fictitious drag coefficient in the vegetated region. Papke and Battiato (2013) and Battiato and Rubol (2014) have shown that a sufficiently dense canopy can be approximated as a rigid homogeneous porous medium and modelled by a generalized Darcy's law, proposing a new strategy to analyze these kinds of environmental flows. In this section we try to make a further step forward by considering the canopy as a porous and deformable (as opposed to rigid) medium, using the continuum model, similarly to Hsieh and Shiu (2006); we note, however, that the latter authors did not have knowledge of the effective coefficients of the model equations. The FPEL equations are here used for a range of parameters beyond those which have led to the scalings presented in Appendix A. In particular, vegetated flows have typically large porosities and display significant fluid inertial effect. We proceed nonetheless, with the limitations well in mind but strong of the positive feedback which a similar approach (in the simpler, rigid limit) has received[3].

The experimental setup developed by Ghisalberti and Nepf (2002), meant to reproduce the behavior of oceanic seagrass meadows, is considered. Artificial seagrass, with characteristics similar to the real one (blades made from a polyethylene film with $\rho_s = 920\,kg/m^3$ and Young's modulus $E = 3.0 \times 10^8\,Pa$), is placed at the bottom of a flume and a unidirectional water flow is generated by gravity over and through the blades. The dimensions of each blade are: thickness $t = 10^{-4}\,m$, width $w = 3 \times 10^{-3}\,m$ and height $h = 0.127\ m$; the mean spacing between successive blades is 0.023 m, yielding a porosity which exceeds 0.99. The hydraulic diameter of the blades can be computed to be equal to 1.94×10^{-4}; for the geometrical arrangement of cylindrical inclusions considered here a porosity equal to that of the experimental set up is realized when $l = 8.6 \times 10^{-4}\ m$.

Several experimental configurations have been tested by Ghisalberti and Nepf and, for certain parameters of the flow, the onset of *monami* waves has been observed. In such cases the amplitude of the wave and the vortex mechanics have been evaluated. We focus on case B in Ghisalberti and Nepf (2002) for which $\mathrm{Re}_L = \rho_f \bar{U} L/\mu \sim 3.6 \times 10^4$, with $\bar{U} = 5.66 \times 10^{-2}\ m/s$ the water

---

[3] See "Editor Highlight" on the paper by Zampogna et al. (2016), http://agupubs.onlinelibrary.wiley.com/hub/article/10.1002/2016WR018915/editor-highlight/

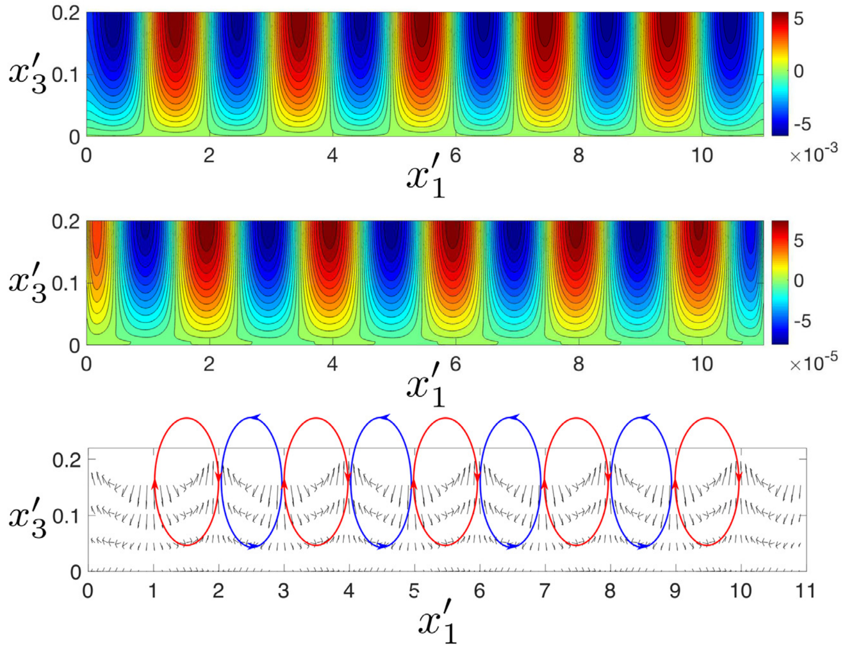

Fig. 18. Horizontal and vertical components of the displacement vector (first two frames) and vector representation of the effective velocity (third frame) at the same temporal instant of Fig. 17. Clockwise and counterclockwise vortices, centered at the interface between canopy and free fluid region, are sketched in red and blue to guide the eye. Figures not to scale. (For interpretation of the references to colour in this figure legend, the reader is referred to the web version of this article.)

velocity above the vegetated layer. The measured dimensional period of the monami is 224 s for a wavelength of $2L = 1.31\,m$ (giving a phase speed slightly smaller than $\bar{U}$). With these data we have $\epsilon = l/L = 1.32 \times 10^{-3}$ and the velocity through the canopy is $U = 6.53 \times 10^{-3}\,m/s$, yielding a microscopic Reynolds number of order one, so that the theory - as developed here - is formally not applicable.

It is however interesting to see whether a complex motion, such as a monami wave, shows up in the displacement field of the poroelastic medium and how the disturbance through the canopy can propagate. For our purposes it is not necessary to consider the macroscopic fluid-structure interaction problem, described previously by the introduction of conditions (18), (19) and (20) and we thus simulate only the poroelastic domain. The PEL model is solved over a rectangular elongated computational box of $7.2\,m \times 0.127\,m$, corresponding to the whole vegetated region in the recirculating flume of Ghisalberti and Nepf (2002). The flow field is assumed to undergo the observed monami effect, and this is borne by the conditions imposed at the upper boundary of the computational box. The complete set of boundary conditions used in the computational configuration are summarized in Fig. 17 together with a snapshot in time of the displacement field; they are:

- a Neumann inlet-outlet condition for the displacement of the homogeneous structure at the vertical boundaries of the domain
$$\frac{\partial v_1}{\partial x'_1} = \frac{\partial v_3}{\partial x'_1} = 0; \tag{28}$$
- a Neumann inlet-outlet condition for the horizontal fluid velocity at the vertical boundaries of the domain; in terms of pressure, this means
$$\frac{\partial^2 p}{\partial x'^2_1} = 0; \tag{29}$$
- a Dirichlet condition to force to zero the displacement at the bottom of the flume,
$$v_1 = v_3 = 0; \tag{30}$$
- a Neumann condition for the normal stresses at Γ_I
$$\frac{\partial^2 v_1}{\partial x'^2_3} = \frac{\partial^2 v_3}{\partial x'^2_3} = 0; \tag{31}$$
- the horizontal and vertical velocities are travelling waves and this can be achieved by imposing the following conditions for the pressure at Γ_I:
$$p = -\alpha \cos(kx'_1 - \omega t) \tag{32}$$
and
$$\mathcal{K}_{33} \frac{\partial^2 p}{\partial x'^2_3} - \mathcal{K}_{11} k^2 p = \frac{\theta}{\epsilon^2 \mathrm{Re}_L} \left(\frac{\partial \dot{v}_1}{\partial x'_1} + \frac{\partial \dot{v}_3}{\partial x'_3} \right). \tag{33}$$

Eq. (33)is necessary to satisfy continuity at Γ_I and can be deduced by substituting Eq. (32) into Eq. (17) and taking the divergence. The parameters k and ω are known from the experiments and, in dimensionless form, are $k = \pi$ and $\omega = 2.02$. The amplitude $\alpha = 10$ is chosen in order for the velocity to be of the order of that measured within the canopy. The remaining important parameter which has to be set is the Cauchy number, which is $\mathrm{Ca} = \rho_f \bar{U}^2 / E = 1.07 \times 10^{-8}$.

We already know from Hoffmann et al. (2004) that the microscopic inclusions must be connected along all directions for a collective movement of the PEL to arise. We thus consider linked structures, as done in the previous section, with $r_c/r = 0.4$, despite the absence in the real physical problem of such connections. To use a structure as close as possible to that of the experiments, we take the values for the effective tensors valid for the case of linked cylinders, with porosity $\theta = 0.99$. The corresponding values of $\mathbb{C}_{ijkl}$ and α_{ij} are available from Fig. 9, while $\mathcal{K}_{11} = 0.15$ and $\mathcal{K}_{33} = 0.18$ (Zampogna and Bottaro, 2016). Travelling vortical structures arise in both velocity and displacement fields. Fig. 17 shows that the periodicity of the vortices $2\pi/k = 2$, imposed as a pressure condition at Γ_I, is maintained by the displacement field, which is perfectly synchronized with the motion of the fluid (compare Fig. 17 and the third frame of Fig. 18). The flow vortices, as observed by Ghisalberti and Nepf (2002), are approximately elliptical in cross-section and expand in the whole

V_{PEL}. A snapshot of the displacement field within the whole PEL is displayed in the top two frames of Fig. 18.

In the experiments, the maximum deflection of the canopy is about 10% of its height, while our poroelastic medium shows a maximum horizontal displacement which is about half, for the same structural stiffness. This is probably related to the parameters of the experiments, to the different solid skeletons present in the two configurations (blades versus connected cylinders) and to the use of a theory based on linear elastic equations. Future work should address the issue of large deformations by the use of nonlinear poroelasticity since, as recently shown by Minn et al. (2016), the errors committed using a theory based on linear poroelasticity in phenomena where the kinematics of the solid skeleton is affected by nonlinearities can be very significant. For the time being we must thus satisfy ourselves with the qualitative agreement observed.

5. Concluding remarks

The present work describes a model to study the interactions between a fluid and a poroelastic layer, in the linear elasticity limit. The paper completes the work by Lācis et al. (2017), where the Stokes limit was treated and validated, by addressing macroscopic configurations for which inertia in the free-fluid region is not negligible. The equations posed here are based on two nested points of view: a microscopic and a macroscopic one. From the coupling of these two points of view significial physical quantities arise: the *effective elasticity tensor* $\mathbb{C}_{ijkl}$ and the *permeability tensor* $\mathcal{K}_{ij}$. Others quantities found, the *effective fluid volume fraction,* α_{ij} and the *bulk compliance of the solid skeleton,* β, describe mainly the variation of porosity due to the deformation of the microscopic skeleton and its compressibility.

The detailed parametric study performed for the microscale problems points to a behavior coherent with fundamentals principles of solid mechanics. The symmetries of the effective elasticity tensor are respected on the basis of the classification of the type of material chosen and on the shape of the skeleton (Cowin, 2013). The values of $\mathbb{C}_{ijkl}$ for non-porous ($\theta = 0$) materials are recovered. Since the only restrictions required for the type of material and for its shape are weak compressibility and connectivity of the skeleton in each direction, the model could be used, in the limit of small deformations, for a reasonably wide range of materials.

This work is but a first step in the development of a complete theory capable to address the macroscopic interactions between a fluid region and a poroelastic medium saturated by a fluid. The main achievement has been that of providing a complete characterization of the microscopic tensors needed for the successive macroscopic study. Two large-scale configurations have been considered and have provided a first test of the theory under particularly straining conditions, considering that the analysis carried out leads to equations which are formally valid only for microscopic Reynolds numbers of order ϵ or smaller. The applications examined – though interesting in their own right – permit to test the equations without representing yet a validation of the model. Hopefully, this work will stimulate future experimental activities with poroelastic materials under conditions for which the hypotheses of the present theory are satisfied. This should not be too difficult, even at large Reynolds numbers, provided the poroelastic medium is characterized by a microscale l sufficiently small.

Appendix A. Development of the interior model

We describe here the mathematical foundations of the continuum model formed by Eqs. (10) and (17) supplied with the microscopic problems (11) and (16). The homogenization technique is applied to (2), (5) and (6), with Eq. (8) as microscopic interface condition between the two phases. The approach follows that outlined by Mei and Vernescu (2010) for the case of *quasi-static* poroelasticity.

A1. Scaling relations

First of all, we need to understand the order (in ϵ) of each term in the dimensional governing equations. If U, $\mathcal{V}$ and T_S are the fluid velocity, solid displacement and solid time scales, respectively, from Eq. (8) it is:

$$U \sim \frac{\mathcal{V}}{T_S}. \tag{A.1}$$

We use Young's modulus of elasticity, E, to scale the elastic tensor and denote by P the pressure scale. If we assume that macroscopic solid stresses in the poroelastic medium are balanced by fluid pressure (cf. Mei and Vernescu, 2010), we have

$$E\frac{Pl^2}{\mu L^2}T_S \sim P, \tag{A.2}$$

provided that macroscopic pressure forces are equilibrated by microscopic viscous dissipation i.e.

$$\frac{P}{L} \sim \frac{\mu U}{l^2}. \tag{A.3}$$

Thus, the solid time scale can be chosen as

$$T_S = \epsilon^{-2}\frac{\mu}{E}. \tag{A.4}$$

Furthermore, from (2) we define T_S so that

$$\frac{\rho_s}{T_S^2} = \frac{E}{L^2}, \tag{A.5}$$

provided that solid inertia is of comparable magnitude as the solid stress over the macroscale. Combining Eqs. (A.4) and (A.5) we obtain:

$$\epsilon^{-2} = \frac{\rho_s E l^2}{\mu^2}. \tag{A.6}$$

Relation (A.3) implies that the fluid velocity scale can be written as

$$U = \epsilon\frac{Pl}{\mu}. \tag{A.7}$$

Using this last equation together with Eqs. (A.1) and (A.4) we can define the solid displacement scale:

$$\mathcal{V} = \epsilon\frac{PL^2}{El} = \frac{PL}{E}. \tag{A.8}$$

We are now ready to introduce the relations between the dimensional and dimensionless variables (the latter without hat); in principle, two adimensional times can be introduced, one for the fluid, $t_f = U\hat{t}/l$, and one for the solid, with $t_s = \epsilon^2 E\hat{t}/\mu$. Furthermore:

$$\hat{\mathbf{x}} = l\mathbf{x}, \quad \hat{p} = Pp, \quad \hat{\mathbf{u}} = \epsilon\frac{Pl}{\mu}\mathbf{u}, \quad \hat{\mathbf{v}} = \frac{PL}{E}\mathbf{v}. \tag{A.9}$$

Substituting these definitions in the momentum equation for the fluid phase we have:

$$\epsilon\mathrm{Re}\left(\frac{\partial u_i}{\partial t_f} + u_j\frac{\partial u_i}{\partial x_j}\right) = -\frac{\partial p}{\partial x_i} + 2\epsilon\frac{\partial \varepsilon_{ij}(\mathbf{u})}{\partial x_j}, \tag{A.10}$$

where $\mathrm{Re} = (\rho_f U l)/\mu$. Applying the same procedure to the equation for the solid we obtain:

$$\epsilon^2\frac{\partial^2 v_i}{\partial t_s^2} = \frac{\partial \sigma_{ij}}{\partial x_j} \quad \text{on } V_s. \tag{A.11}$$

The boundary condition on the normal stresses becomes:

$$-p\,n_i + 2\epsilon\,\varepsilon_{ij}(\mathbf{u})n_j = \left[\frac{1}{\epsilon}C_{ijkl}\varepsilon_{kl}(\mathbf{v})\right]n_j \quad \text{on } \Gamma. \tag{A.12}$$

The continuity equation for the fluid (6), the boundary condition (8) and V-periodicity remain unchanged.

A2. Multiple scales analysis

At this point we can perform a multiple scale expansion recalling the fast and slow variables, $\mathbf{x}$ and $\mathbf{x}' = \epsilon\mathbf{x}$, respectively, and the expansions

$$f = f^{(0)} + \epsilon f^{(1)} + \epsilon^2 f^{(2)} + \dots \quad \text{where } f = \{u_i, v_i, p, \Sigma_{ij}, \sigma_{ij}\}. \tag{A.13}$$

Moreover, we note that the strain tensor (for either the solid or the fluid) becomes

$$\varepsilon_{ij} + \epsilon\varepsilon'_{ij} \tag{A.14}$$

where

$$\varepsilon_{ij}(w) = \frac{1}{2}\left(\frac{\partial w_i}{\partial x_j} + \frac{\partial w_j}{\partial x_i}\right) \tag{A.15}$$

and

$$\varepsilon'_{ij}(w) = \frac{1}{2}\left(\frac{\partial w_i}{\partial x'_j} + \frac{\partial w_j}{\partial x'_i}\right). \tag{A.16}$$

A3. Small Reynolds number

Using Eqs. (A.13) and (A.14), and assuming that the microscale Reynolds number, Re, is $\mathcal{O}(\epsilon)$, we obtain at orders 0 and 1 in ϵ the following system for the fluid:

$$\frac{\partial u_i^{(0)}}{\partial x_i} = 0, \tag{A.17}$$

$$\frac{\partial u_i^{(1)}}{\partial x_i} + \frac{\partial u_i^{(0)}}{\partial x'_i} = 0, \tag{A.18}$$

$$0 = -\frac{\partial p^{(0)}}{\partial x_i}, \tag{A.19}$$

$$0 = \frac{\partial \Sigma_{ij}^{(0)}}{\partial x'_j} + \frac{\partial \Sigma_{ij}^{(1)}}{\partial x_j} = -\frac{\partial p^{(1)}}{\partial x_i} - \frac{\partial p^{(0)}}{\partial x'_i} + \frac{\partial^2 u_i^{(0)}}{\partial x_j \partial x_j}, \tag{A.20}$$

on V_f, and for the solid at order 0, 1 and 2:

$$\frac{\partial \sigma_{ij}^{(0)}}{\partial x_j} = 0, \tag{A.21}$$

$$0 = \frac{\partial \sigma_{ij}^{(1)}}{\partial x_j} + \frac{\partial \sigma_{ij}^{(0)}}{\partial x'_j}, \tag{A.22}$$

$$\frac{\partial^2 v_i^{(0)}}{\partial t_s^2} = \frac{\partial \sigma_{ij}^{(2)}}{\partial x_j} + \frac{\partial \sigma_{ij}^{(1)}}{\partial x'_j}, \tag{A.23}$$

on V_s, plus the boundary conditions on Γ:

$$u_i^{(0)} = \frac{\partial v_i^{(0)}}{\partial t_s}, \tag{A.24}$$

$$u_i^{(1)} = \frac{\partial v_i^{(1)}}{\partial t_s}, \tag{A.25}$$

$$\sigma_{ij}^{(0)}n_j = 0, \tag{A.26}$$

$$\sigma_{ij}^{(1)}n_j = \Sigma_{ij}^{(0)}n_j = -p^{(0)}n_i, \tag{A.27}$$

$$\sigma_{ij}^{(2)}n_j = \Sigma_{ij}^{(1)}n_j. \tag{A.28}$$

It is useful to specify the form of the tensors σ and Σ at the two leading powers in ϵ:

$$\sigma_{ij}^{(0)} = C_{ijkl}(\varepsilon_{kl}(\mathbf{v}^{(0)})), \tag{A.29}$$

$$\sigma_{ij}^{(1)} = C_{ijkl}(\varepsilon_{kl}(\mathbf{v}^{(1)})) + C_{ijkl}(\varepsilon'_{kl}(\mathbf{v}^{(0)})), \tag{A.30}$$

$$\Sigma_{ij}^{(0)} = -p^{(0)}\delta_{ij}, \tag{A.31}$$

$$\Sigma_{ij}^{(1)} = -p^{(1)}\delta_{ij} + 2\varepsilon_{ij}(\mathbf{u}^{(0)}). \tag{A.32}$$

We now observe that, from Eq. (A.19), the pressure at leading order is independent of the microscale, i.e. $p^{(0)} = p^{(0)}(\mathbf{x}', t_f)$; the system formed by (A.21) and (A.26) implies that

$$\sigma_{ij}^{(0)} = 0 \;\forall\; i, j \quad \text{i.e. } C_{ijkl}(\varepsilon_{kl}(\mathbf{v}^{(0)})) = 0 \;\forall\; i, j, \tag{A.33}$$

and from this we have

$$\varepsilon_{kl}(\mathbf{v}^{(0)}) = 0 \;\forall\; k, l \tag{A.34}$$

which implies that also the solid displacement at leading order is not a function of the microscale, i.e. $\mathbf{v}^{(0)} = \mathbf{v}^{(0)}(\mathbf{x}', t_s)$.

A4. The effective elasticity tensor

Coupling the $\mathcal{O}(\epsilon)$ solid momentum Eq. (A.22) with the boundary condition (A.27) we obtain a system which, using (A.30) and (A.33), can be rewritten in the following way:

$$\frac{\partial}{\partial x_j}\left\{C_{ijkl}\left[\varepsilon_{kl}(\mathbf{v}^{(1)}) + \varepsilon'_{kl}(\mathbf{v}^{(0)})\right]\right\} = 0 \quad \text{on } V_s, \tag{A.35}$$

$$\left\{C_{ijkl}\left[\varepsilon_{kl}(\mathbf{v}^{(1)}) + \varepsilon'_{kl}(\mathbf{v}^{(0)})\right]\right\}n_j = -p^{(0)}n_i \quad \text{on } \Gamma, \tag{A.36}$$

plus V-periodicity. Since the system above is a linear differential equation for $\mathbf{v}^{(1)}$ forced by $\mathbf{v}^{(0)}$ and $p^{(0)}$, we formally express $\mathbf{v}^{(1)}$ in terms of $\mathbf{v}^{(0)}$ and $p^{(0)}$:

$$v_i^{(1)}(\mathbf{x}, \mathbf{x}', t_s) = \chi_i^{pq}(\mathbf{x})\varepsilon'_{pq}(\mathbf{v}^{(0)})(\mathbf{x}', t_s) - \eta_i(\mathbf{x})p^{(0)}(\mathbf{x}', t_s) \quad \text{on } V_s, \tag{A.37}$$

where $\boldsymbol{\chi}$ is a third order tensor and $\boldsymbol{\eta}$ a vector. The fluid pressure at the leading order $p^{(0)}$ can be formally expressed as a function of t_s, related to t_f on account of $t_f = \epsilon^{-2}\frac{\rho_f}{\rho_s}\frac{\text{Ca}}{\text{Re}}t_s$. Substituting (A.37) into (A.35) and (A.36) we have:

$$\frac{\partial}{\partial x_j}\left\{C_{ijkl}\left[\varepsilon_{kl}(\boldsymbol{\chi}^{pq})\varepsilon'_{pq}(\mathbf{v}^{(0)})\right] - C_{ijkl}\left[\varepsilon_{kl}(\boldsymbol{\eta})p^{(0)}\right] + \right.$$
$$\left. + C_{ijkl}\left[\varepsilon'_{kl}(\mathbf{v}^{(0)})\right]\right\} = 0 \quad \text{on } V_s, \tag{A.38}$$

$$\left\{C_{ijkl}\left[\varepsilon_{kl}(\boldsymbol{\chi}^{pq})\varepsilon'_{pq}(\mathbf{v}^{(0)})\right] - C_{ijkl}\left[\varepsilon_{kl}(\boldsymbol{\eta})p^{(0)}\right] + \right.$$
$$\left. + C_{ijkl}\left[\varepsilon'_{kl}(\mathbf{v}^{(0)})\right]\right\}n_j = -p^{(0)}n_i \quad \text{on } \Gamma. \tag{A.39}$$

A solution of this system can be found by solving the two systems in (11). The averaging operator in Eq. (9) can be written in adimensional form as

$$\langle f_p \rangle = \frac{1}{|V|}\int_{V_p} f_p\, dV, \tag{A.40}$$

where the function f_p is defined on V_p and the subscript p means either the fluid (f) or the solid (s) phase. From this moment on we will not distinguish between the solid or fluid phase averaging unless the distinction is ambiguous. Our target is to deduce a set of equations to determine the solution up to order ϵ. In order to do this we can take the solid-phase average to express the solid stress:

$$\begin{aligned}\langle\sigma_{ij}^{(1)}\rangle &= \\ &= \langle C_{ijkl}\ \varepsilon_{kl}(\mathbf{v}^{(1)})\rangle + \langle C_{ijkl}\rangle\varepsilon'_{kl}(\mathbf{v}^{(0)}) = \\ &= \big[\langle C_{ijkl}\ \varepsilon_{kl}(\boldsymbol{\chi}^{pq})\rangle + \langle C_{ijkl}\rangle\delta_{kp}\delta_{lq}\big]\varepsilon'_{pq}(\mathbf{v}^{(0)}) \\ &\quad -\langle C_{ijkl}\ \varepsilon_{kl}(\boldsymbol{\eta})\rangle p^{(0)} = \\ &= \mathbb{C}_{ijpq}\ \varepsilon'_{pq}(\mathbf{v}^{(0)}) - \langle C_{ijkl}\ \varepsilon_{kl}(\boldsymbol{\eta})\rangle p^{(0)},\end{aligned} \tag{A.41}$$

where $\mathbb{C}_{ijpq}$ is given in (12).

A5. Momentum balance for the composite

Eq. (A.41)is the macroscale Hooke's law in the solid phase forced by the fluid pressure. To deduce the momentum equation for the composite we can define a new tensor

$$T_{ij} = \begin{cases}\Sigma_{ij} & \text{on } V_f \\ \epsilon^{-1}\sigma_{ij} & \text{on } V_s.\end{cases} \tag{A.42}$$

where σ is divided by ϵ because we take into account the scaling relation (A.12) between σ and Σ. It is useful at this point, to compute the average of $T_{ij}^{(0)}$, i.e. $\langle T_{ij}^{(0)}\rangle = \int_V T_{ij}^{(0)}\,dV/|V|$:

$$\begin{aligned}\langle T_{ij}^{(0)}\rangle &= \langle\sigma_{ij}^{(1)}\rangle + \langle\Sigma_{ij}^{(0)}\rangle = \langle\sigma_{ij}^{(1)}\rangle - \theta p^{(0)}\delta_{ij} = \\ &= \big[\langle C_{ijkl}\ \varepsilon_{kl}(\boldsymbol{\chi}^{pq})\rangle + \langle C_{ijkl}\rangle\delta_{kp}\delta_{lq}\big]\varepsilon'_{pq}(\mathbf{v}^{(0)}) \\ &\quad -(\langle C_{ijkl}\ \varepsilon_{kl}(\boldsymbol{\eta})\rangle + \theta\delta_{ij})p^{(0)} = \\ &= \mathbb{C}_{ijpq}\ \varepsilon'_{pq}(\mathbf{v}^{(0)}) - \alpha'_{ij}p^{(0)},\end{aligned} \tag{A.43}$$

where α'_{ij} is defined by

$$\alpha'_{ij} = \theta\delta_{ij} + \langle C_{ijkl}\ \varepsilon_{kl}(\boldsymbol{\eta})\rangle. \tag{A.44}$$

Adding the averages of (A.20) and (A.23) we get

$$\langle\frac{\partial^2 v_i^{(0)}}{\partial t_s^2}\rangle = \langle\frac{\partial T_{ij}^{(0)}}{\partial x'_j}\rangle + \langle\frac{\partial\Sigma_{ij}^{(1)}}{\partial x_j}\rangle + \langle\frac{\partial\sigma_{ij}^{(2)}}{\partial x_j}\rangle. \tag{A.45}$$

Observing that we can exchange integral and derivative only if the integration domain and variables do not depend on the differentiation variable, we obtain

$$(1-\theta)\frac{\partial^2 v_i^{(0)}}{\partial t_s^2} = \frac{\partial\langle T_{ij}^{(0)}\rangle}{\partial x'_j} + \frac{1}{|V|}\int_{V_f}\frac{\partial\Sigma_{ij}^{(1)}}{\partial x_j}\,dV + \frac{1}{|V|}\int_{V_s}\frac{\partial\sigma_{ij}^{(2)}}{\partial x_j}\,dV,$$

which, using Gauss theorem, becomes

$$(1-\theta)\frac{\partial^2 v_i^{(0)}}{\partial t_s^2} = \frac{\partial\langle T_{ij}^{(0)}\rangle}{\partial x'_j} + \frac{1}{|V|}\int_\Gamma\left(\sigma_{ij}^{(2)} - \Sigma_{ij}^{(1)}\right)n_j\,d\Omega. \tag{A.46}$$

The last integral in the equation above is zero by the boundary condition (A.28), so that the average momentum balance of the composite can be rewritten as

$$(1-\theta)\frac{\partial^2 v_i^{(0)}}{\partial t_s^2} = \frac{\partial}{\partial x'_j}\big[\mathbb{C}_{ijpq}\varepsilon'_{pq}(\mathbf{v}^{(0)}) - \alpha'_{ij}p^{(0)}\big]. \tag{A.47}$$

The solution of Eq. (A.47) can be addressed after that of the equations for $\boldsymbol{\chi}$ and $\boldsymbol{\eta}$ which yield $\mathbb{C}_{ijkl}$.

A6. Continuity equation for the composite

Another equation is deduced using the continuity equation for the fluid at order ϵ. Let us take the fluid-phase average of (A.18):

$$\langle\frac{\partial u_i^{(0)}}{\partial x'_i}\rangle = -\frac{1}{|V|}\int_{V_f}\frac{\partial u_i^{(1)}}{\partial x_i}\,dV. \tag{A.48}$$

As before we can exchange derivative and integral; using Gauss theorem, we obtain that the equation above is equivalent to

$$\begin{aligned}\frac{\partial\langle u_i^{(0)}\rangle}{\partial x'_i} &= \frac{1}{|V|}\int_\Gamma u_i^{(1)}n_i\,d\Omega = \frac{1}{|V|}\int_\Gamma\frac{\partial v_i^{(1)}}{\partial t_s}n_i\,d\Omega \\ &= \frac{1}{|V|}\int_{V_s}\frac{\partial}{\partial x_i}\frac{\partial v_i^{(1)}}{\partial t_s}\,dV = \langle\frac{\partial}{\partial x_i}\frac{\partial v_i^{(1)}}{\partial t_s}\rangle,\end{aligned} \tag{A.49}$$

by the boundary condition (A.25). Eq. (A.37) tells us that

$$\begin{aligned}\langle\frac{\partial}{\partial x_i}\frac{\partial v_i^{(1)}}{\partial t_s}\rangle &= \langle\frac{\partial}{\partial x_i}\frac{\partial}{\partial t_s}\big[\chi_i^{pq}(\mathbf{x})\varepsilon'_{pq}(\mathbf{v}^{(0)})(\mathbf{x}',t_s) - \eta_i(\mathbf{x})p^{(0)}(\mathbf{x}',t_s)\big]\rangle \\ &= \langle\frac{\partial}{\partial x_i}\chi_i^{pq}(\mathbf{x})\varepsilon'_{pq}\left(\frac{\partial\mathbf{v}^{(0)}}{\partial t_s}\right)(\mathbf{x}',t_s)\rangle \\ &\quad -\langle\frac{\partial}{\partial x_i}\eta_i(\mathbf{x})\frac{\partial p^{(0)}}{\partial t_s}(\mathbf{x}',t_s)\rangle = \\ &= \langle\frac{\partial\chi_i^{pq}}{\partial x_i}\rangle\varepsilon'_{pq}\left(\frac{\partial\mathbf{v}^{(0)}}{\partial t_s}\right) - \langle\frac{\partial\eta_i}{\partial x_i}\rangle\frac{\partial p^{(0)}}{\partial t_s}.\end{aligned} \tag{A.50}$$

The only time variable present is relative to the solid, i.e. $t_s = \hat{t}/T_S$, with $T_S = \frac{\rho_S l^2}{\mu}$. Substituting the equation above in (A.49) we obtain a relation between the solid stress and the pressure:

$$\frac{\partial\langle u_i^{(0)}\rangle}{\partial x'_i} = \langle\frac{\partial\chi_i^{pq}}{\partial x_i}\rangle\varepsilon'_{pq}\left(\frac{\partial\mathbf{v}^{(0)}}{\partial t_s}\right) - \langle\frac{\partial\eta_i}{\partial x_i}\rangle\frac{\partial p^{(0)}}{\partial t_s}. \tag{A.51}$$

Also this equation can be solved, once we know $\boldsymbol{\chi}$ and $\boldsymbol{\eta}$.

A7. Momentum equation for the effective flow

In order to obtain a momentum equation for the fluid phase we consider the problem formed by (A.17), (A.20), the boundary condition (A.24) plus periodicity over V. This problem can be viewed as a Stokes problem for $\mathbf{u}^{(0)}$ and $p^{(1)}$ forced by the gradient of $p^{(0)}$ and by $\partial v_j^{(0)}/\partial t_s$, quantities defined only over the macroscale $\mathbf{x}'$, so that the most general solution takes the form:

$$u_i^{(0)} = -K_{ij}\frac{\partial p^{(0)}}{\partial x'_j} + H_{ij}\frac{\partial v_j^{(0)}}{\partial t_s} \quad \text{and} \quad p^{(1)} = -A_j\frac{\partial p^{(0)}}{\partial x'_j} + B_j\frac{\partial v_j^{(0)}}{\partial t_s}. \tag{A.52}$$

Substituting into Eqs. (A.17), (A.20) and (A.24) we obtain

$$\frac{\partial H_{ij}}{\partial x_i}\frac{\partial v_j^{(0)}}{\partial t_s} = \frac{\partial K_{ij}}{\partial x_i}\frac{\partial p^{(0)}}{\partial x_j}, \tag{A.53}$$

$$\left(\frac{\partial B_j}{\partial x_i} - \frac{\partial^2 H_{ij}}{\partial x_k\partial x_k}\right)\frac{\partial v_j^{(0)}}{\partial t_s} = \left(\frac{\partial A_j}{\partial x_i} - \delta_{ij} - \frac{\partial K_{ij}}{\partial x_k\partial x_k}\right)\frac{\partial p^{(0)}}{\partial x'_j}, \tag{A.54}$$

and

$$\left(H_{ij} - \delta_{ij}\right)\frac{\partial v_j^{(0)}}{\partial t_s} = K_{ij}\frac{\partial p^{(0)}}{\partial x'_j} \quad \text{on } \Gamma. \tag{A.55}$$

A solution of this problem can be found imposing that left- and right-hand-sides of Eqs. (A.53) and (A.54) vanish, yielding two different problems which must be solved in the unit cell over V_f:

$$\frac{\partial A_j}{\partial x_i} - \frac{\partial K_{ij}}{\partial x_k\partial x_k} = \delta_{ij}, \quad \frac{\partial K_{ij}}{\partial x_i} = 0, \quad K_{ij} = 0 \quad \text{on } \Gamma, \tag{A.56}$$

and

$$\frac{\partial B_j}{\partial x_i} - \frac{\partial H_{ij}}{\partial x_k \partial x_k} = 0, \quad \frac{\partial H_{ij}}{\partial x_i} = 0, \quad H_{ij} = \delta_{ij} \quad \text{on } \Gamma. \tag{A.57}$$

In order to guarantee unicity of the solution, since only the gradients of A_j and B_j appear in (A.56) and (A.57), we impose $\langle A_j \rangle = 0$ and $\langle B_j \rangle = 0$. The solution of (A.57) is simply $H_{ij} = \delta_{ij}$; the volume average of K_{ij} and H_{ij}, denoted, respectively, as $\mathcal{K}_{ij}$ and $\mathcal{H}_{ij}$ are:

$$\mathcal{K}_{ij} = \langle K_{ij} \rangle \quad \text{and} \quad \mathcal{H}_{ij} = \langle H_{ij} \rangle = \theta \delta_{ij}. \tag{A.58}$$

Finally, the volume average of Eq. (A.52) for the fluid phase is

$$\langle u_i^{(0)} \rangle - \theta \frac{\partial v_i^{(0)}}{\partial t_s} = -\mathcal{K}_{ij} \frac{\partial p^{(0)}}{\partial x'_j}, \tag{A.59}$$

$$\langle p^{(1)} \rangle = -\mathcal{A}_j \frac{\partial p^{(0)}}{\partial x'_j} + \mathcal{B}_j \frac{\partial v_j^{(0)}}{\partial t_s}. \tag{A.60}$$

Eq. (A.59) is Darcy's law for the unknown $\langle u_i^{(0)} \rangle - \theta \partial v_i^{(0)} / \partial t_s$, which is the average velocity of the fluid relative to the solid.

A8. Adimensionalizing the equations with fluid-related scales

Re-normalizing length and displacement with respect to L, pressure with respect to $\rho_f \bar{U}^2$, time with respect to $L/\bar{U}$, where $\bar{U}$ is the macroscopic velocity scale in the free-fluid region, we obtain three fundamentals equations, i.e.

-the first equation of system (10);

-the following equation

$$\frac{\partial \langle u_i^{(0)} \rangle}{\partial x'_i} = \langle \frac{\partial \chi_i^{pq}}{\partial x_i} \rangle \varepsilon'_{pq}(\dot{\mathbf{v}}^{(0)}) - \langle \frac{\partial \eta_i}{\partial x_i} \rangle \mathrm{Ca}\, \dot{p}^{(0)}; \tag{A.61}$$

-Eq. (17);

a dot over a variable denotes differentiation with respect to the only dimensionless time variable present. Substituting (17) into (A.61) and using the definition (13), we obtain the second equation of system (10).

Appendix B. The interface conditions

In order to find the effective interface coefficients defined in (21) and (22), microscopic problems must be solved within the interface cell introduced in Section 3.2. The main idea to deduce these problems, which is explained in Lācis and Bagheri (2016) and in Lācis et al. (2017) for both rigid and elastic porous media, is to perform a multiple scale expansion of the physical quantities above (denoted with $\cdot^+$) and below ($\cdot^-$) the macroscopic interface Γ_I and match the two solutions. The coefficients and the respective problems derived using this procedure are given below. The microscopic permeability tensor $\tilde{K}_{ij}^{\pm}$ and the vector $A_j^{\pm}$ solve

$$\frac{\partial A_j^+}{\partial x_i} - \frac{\partial \tilde{K}_{ij}^+}{\partial x_k \partial x_k} = 0, \quad \frac{\partial \tilde{K}_{ij}^+}{\partial x_i} = 0, \tag{B.1}$$

$$\begin{gathered} \frac{\partial A_j^-}{\partial x_i} - \frac{\partial \tilde{K}_{ij}^-}{\partial x_k \partial x_k} = \delta_{ij}, \quad \frac{\partial \tilde{K}_{ij}^-}{\partial x_i} = 0, \\ \tilde{K}_{ij}^- = \tilde{K}_{ij}^+ \text{on } \Gamma_I \\ \left(-A_k^- \delta_{ij} + \frac{\partial \tilde{K}_{ik}^-}{\partial x_j} + \frac{\partial \tilde{K}_{jk}^-}{\partial x_i} \right) n_j = \left(-A_k^+ \delta_{ij} + \frac{\partial \tilde{K}_{ik}^+}{\partial x_j} + \frac{\partial \tilde{K}_{jk}^+}{\partial x_i} \right) n_j \text{on } \Gamma_I, \end{gathered} \tag{B.2}$$

where, in contrast to the previous problem, instead of surface forcing on the boundaries of the solid material, now we have volume forcing in the whole fluid volume within the microscopic cell at the interface. Finally, the interface problem for the slip tensor $L_{ijk}^{\pm}$ and the tensor $P_{ij}^{\pm}$ is

$$\frac{\partial P_{jk}^+}{\partial x_i} - \frac{\partial L_{ijk}^+}{\partial x_n \partial x_n} = 0, \quad \frac{\partial L_{ijk}^+}{\partial x_i} = 0, \tag{B.3}$$

$$\begin{gathered} \frac{\partial P_{jk}^-}{\partial x_i} - \frac{\partial L_{ijk}^-}{\partial x_n \partial x_n} = 0, \quad \frac{\partial L_{ijk}^-}{\partial x_i} = 0, \\ L_{ijk}^- = L_{ijk}^+ \text{on } \Gamma_I \\ \left(-P_{kl}^- \delta_{ij} + \frac{\partial L_{ikl}^-}{\partial x_j} + \frac{\partial L_{jkl}^-}{\partial x_i} \right) n_j = \left(-P_{kl}^+ \delta_{ij} + \frac{\partial L_{ikl}^+}{\partial x_j} + \frac{\partial L_{jkl}^+}{\partial x_i} \right) n_j \\ + \delta_{ik} n_l \text{on } \Gamma_I, \end{gathered} \tag{B.4}$$

where we have again a surface forcing, which this time is located at the interface between the poroelastic medium and the free fluid, expressed as a stress jump between these two different domains. Once these quantities are calculated, they are rendered macroscopic via Eqs. (21) and (22) and are used in the macroscopic interface condition (20).

Supplementary material

Supplementary material associated with this article can be found, in the online version, at doi:10.1016/j.ijmultiphaseflow.2018.09.006

References

Auriault, J.L., Sanchez-Palencia, E., 1977. Étude du comportement macroscopique d'un milieu poreux saturé déformable. J. de Mécanique 16, 575–603.

Bachmann, T., Klän, S., Baumgartner, W., Klaas, M., Schröder, W., Wagner, H., 2008. Morphometric characterisation of wing feathers of the barn owl tyto alba pratincola and the pigeon columba livia. Front. Zoology 4 (23), 1–15.

Badia, S., Quaini, A., Quarteroni, A., 2009. Coupling Biot and Navier-Stokes equations for modelling fluid-poroelastic media interaction. J. Comp. Phys. 228, 7986–8014.

Battiato, I., Rubol, S., 2014. Single-parameter model of vegetated aquatic flows. Water Res. Res. 50, 6358–6369.

Beavers, G.S., Joseph, D.D., 1967. Boundary condition at a natural permeable wall.. J. Fluid Mech. 30, 197–207.

Biot, M.A., 1955. Theory of elasticity and consolidation for a porous anisotropic solid. J. Appl. Phys. 26 (2), 182–185.

Bukač, M., Yotov, I., Zunino, P., 2015. An operator splitting approach for the interaction between a fluid and a multilayered poroelastic structure. Num. Meth. PDE 31, 1054–1100.

Burridge, R., Keller, J.B., 1981. Poroelasticity equations derived from microstructure. J. Acoustical Soc. America 70 (4), 1140–1146.

Carraro, T., Goll, C., Marciniak-Czochra, A., Mikelić, A., 2013. Pressure jump interface law for the Stokes–Darcy coupling: confirmation by direct numerical simulations. J. Fluid. Mech. 732, 510–536.

Carraro, T., Goll, C., Marciniak-Czochra, A., Mikelić, A., 2015. Effective interface conditions for the forced infiltration of a viscous fluid into a porous medium using homogenization. Comp. Met. App. Mech. Eng. 292, 195–220.

Cowin, S.C., 2013. Continuum mechanics of anisotropic materials. Springer, New York.

De Langre, E., 2008. Effect of wind on plants. Ann. Rev. Fluid Mech. 40, 141–168.

Ghisalberti, M., Nepf, H.M., 2002. Mixing layers and coherent structures in vegetated aquatic flows.. J. Geophys. Res. 107 (3), 1–11.

Ghisalberti, M., Nepf, H.M., 2009. Shallow flows over a permeable medium: the hydrodynamics of submerged aquatic canopies. Transp. Porous Med. 78 (2), 309–326.

Gopinath, A., Mahadevan, L., Elastohydrodynamics of wet bristles, c., brushes, 2011. Proc. Roy. Soc. A 467, 1665–1685.

Hecht, F.H., 2012. New development in freefem++.. J. Numer. Math. 20, 251–265.

Hoffmann, K.H., Botkin, N.D., Starovoitov, V.N., 2004. Homogenization of interfaces between rapidly oscillating fine elastic structures and fluids.. J. App. Maths. 65, 983–1005.

Hornung, U., 1996. Homogenization and porous media. Springer-Verlag, New York.

Hsieh, P.C., Shiu, Y.S., 2006. Analytical solutions for water flow passing over a vegetal area.. Adv. Water Res. 29, 1257–1266.

Jäger, W., Mikelić, A., 1996. On the boundary conditions at the contact interface between a porous medium and a free fluid. Ann. Scuola Norm. Sup. Pisa, Classe Fisiche e Matematiche-Serie IV 23, 403–465.

Jäger, W., Mikelić, A., 2000. On the interface boundary condition of beavers, joseph, and saffman. SIAM J. Math. Anal. 60, 1111–1127.

Jäger, W., Mikelić, A., 2009. Modeling effective interface laws for transport phenomena between an unconfined fluid and a porous medium using homogenization.. Transp. Porous Med. 78, 489–508.

Jäger, W., Mikelić, A., Neuss-Radu, M., 2011. Homogenization limit of a model system for interaction of flow, chemical reactions, and mechanics in cell tissues.. SIAM J. Math. Anal. 43, 1390–1435.

Jones, I.P., 1973. Low reynolds number flow past a porous spherical shell.. Proc. Camb. Philol. Soc. 73, 231–238.

Lācis, U., Bagheri, S., 2016. A framework for computing effective boundary conditions at the interface between free fluid and a porous medium.. J. Fluid. Mech. 812, 866–889.

Lācis, U., Zampogna, G.A., Bagheri, S., 2017. Computational continuum model of poroelastic beds. Proc. Roy. Soc. A 473, 20160932.

Mei, C.C., Vernescu, B., 2010. Homogenization methods for multiscale mechanics. World Scientific, Singapore.

Mikelić, A., Jäger, W., 2000. On the interface boundary condition of beavers. SIAM J. App. Math. 60, 1111–1127. Joseph, and Saffman

Mikelić, A., Wheeler, M.F., 2012. Theory of the dynamic biot-allard equations and their link to the quasi-static biot system. J. Math. Phys. 53, 123702.

Mac Minn, C.W., Dufresne, E.R., Wettlaufer, J.S., 2016. Large deformations of a soft porous material. Phys. Rev. Appl. 5, 044020.

Nepf, H.M., 2012. Flow and transport in regions with aquatic vegetation. Annual Rev. Fluid Mech. 44, 123–142.

Nevard, J., Keller, J.B., 1997. Homogenization of rough boundaries and interfaces.. SIAM J. Appl. Math. 57, 1660–1686.

Nield, D.A., Bejan, A., 2013. Convection in porous media. Springer-Verlag, New York.

Papke, A., Battiato, I., 2013. A reduced complexity model for dynamic similarity in obstructed shear flows.. Geophys. Res. Lett. 40, 3888–3892.

Penta, R., Ambrosi, D., 2013. Effective governing equations for poroelastic growing media. Quart. J. Mech. Appl. Math. 67 (1), 69–91.

Raupach, M.R., Finnigan, J.J., Brunet, Y., 1996. Coherent eddies and turbulence in vegetation canopies: the mixing layer analogy. Bound. Lay. Meteor. 78, 351–382.

Raupach, M.R., Shaw, R.H., 1982. Averaging procedures for flow within vegetation canopies. Bound. Lay. Meteor. 22, 79–90.

Saffman, P.G., 1971. On the boundary condition at the surface of a porous medium.. Stud. Appl. Math. 50, 93–101.

Sarradj, E., Fritzsche, C., Geyer, T., 2011. Silent owl flight: flyover noise measurements. AIAA J., 49 (4), 769–779.

Segur, J.B., Obestan, H.E., 1951. Viscosity of glycerol and its aqueous solutions.. Ind. Eng. Chem. 43, 2117–2120.

Shavit, U., 2009. Transport phenomena at the interface between fluid and porous domains.. Transp. Porous Med. 78, 327–330.

Showalter, R.E., 2003. Poroelastic filtration coupled to stokes flow.. Lect. Notes Pure Appl. Math. 242, 229–244.

Skotheim, J.M., Mahadevan, L., 2004. Dynamics of poroelastic filaments.. Proc. Roy. Soc. Lond. A 460, 1995–2020.

Terzaghi, K., 1936. The shearing resistance of saturated soils.. Proc. First Int. Conf. Soil Mech. Found. Eng. 1, 54–55.

Voigt, W., 1889. Ueber die beziehung zwischen den beiden elasticitatsconstanten isotroper korper. Ann. Phys. 274 (12), 573–587.

Zampogna, G.A., Bottaro, A., 2016. Fluid flow over and through a regular bundle of rigid fibres. J. Fluid Mech. 792, 5–35.

Zampogna, G.A., Bottaro, A., 2017. The PELskin project - part III - a homogenized model of flows over and through dense poroelastic media. Mecc. 52, 1797–1808.

Zampogna, G.A., Pluvinage, F., Kourta, A., Bottaro, A., 2016. Instability of canopy flows. Wat. Res. Res. 52, 5421–5432.